A Displacement-Based Fiber Element to Simulate Interactive Lateral Torsional and Local Buckling in Steel Members

Arka Maity, S.M.ASCE[1]; Amit Kanvinde, M.ASCE[2]; Diego I. Heredia Rosa, S.M.ASCE[3]; Albano de Castro e Sousa[4]; and Dimitrios G. Lignos, M.ASCE[5]

Abstract: Collapse in steel structures is often controlled by loss of load carrying capacity of steel columns due to interactive buckling, which involves interactions between local and global (i.e., lateral and lateral torsional) buckling. Commonly used concentrated plastic hinge or fiber-based elements do not simulate the physics of this response, potentially leading to inaccuracy in performance assessment. A nonlinear fiber-beam-column element [termed the Torsion Fiber Element (TFE)] to simulate monotonic interactive buckling in steel beam-columns is presented. The element, implemented in the OpenSees platform, incorporates St. Venant as well as warping torsion through enrichment of strain interpolation functions, in addition to axial and flexural deformation modes. Local buckling is represented through a softening multiaxial constitutive relationship. The efficacy of this approach is examined by comparing its results against those obtained from continuum finite element simulations as well as experimental data on beam-columns subjected to monotonic loading. The comparisons indicate that the element can functionally represent the physics underlying interactive buckling, resulting in effective prediction of the overall monotonic load-deformation response, as well as internal deformation and stress fields. Limitations of the element in its current form are summarized, along with prospective improvements. **DOI: 10.1061/JSENDH.STENG-11889.** *© 2023 American Society of Civil Engineers.*

Author keywords: Frame elements; Steel beam-columns; Local buckling; Lateral torsional buckling.

Introduction

The performance assessment and design of structures subjected to extreme loads (e.g., seismic, wind, or blast) increasingly rely on the accuracy of model-based simulations of limit states such as collapse. This is enabled by design standards (e.g., ASCE 2017) and guidelines (PEER/ATC 2010) that allow or mandate the use of nonlinear response-history simulations of buildings to evaluate collapse or failure probabilities along with associated acceptance criteria. Sophisticated and robust analysis methods are required to support such model-based assessment/design frameworks; these methods rely on research supplemented by simulation guidance documents for various structural systems in steel (NIST 2017a) and concrete (NIST 2017b). In steel systems, structural collapse is usually the result of loss of member load carrying capacity coupled with the destabilizing effects of gravity.

A dominant member failure mode observed in popular structural steel systems (e.g., columns in moment frames, or multi-tiered braced frames) includes interactions between inelastic lateral torsional buckling and local buckling. One form of buckling may precede and trigger the other (e.g., local buckling diminishes torsional restraint at the ends of the column, triggering lateral torsional buckling), or a coupled failure mode may occur in which both types of buckling happen simultaneously and progressively. In this paper, the term interactive buckling (IB) is used to generically connote all such interactions that lead to loss of member load carrying capacity. Notwithstanding the specific order of events, the physical outcome of IB is a three-dimensional failure mode resulting in loss of member strength. Fig. 1 shows photographs of IB occurring in a column subjected to axial and lateral loads during a test program conducted by Elkady (2016). Fig. 1(a) shows the load-deformation curve of the column tested under major axis bending. Figs. 1(b and c) show the in-plane deformations [at loading instants 1 and 2 shown in Fig. 1(a)], the latter exhibiting local buckling, whereas Fig. 1(d) shows lateral torsional buckling which, along with local buckling, corresponds to the negative slope (and strength loss) observed at loading instant 3. The response shown in Fig. 1 is inherently three-dimensional, with various physical phenomena at play; these include: (1) inelastic torsional response including warping torsion as well as St. Venant type torsion, (2) spread of plasticity along the length and through the cross section, (3) interactions between axial force, biaxial bending, torsion, and shear, and (4) localization of deformation, which typically occurs after local buckling. Similar responses have been noted in other experimental (Chansuk et al. 2021) and computational (Elkady and Lignos 2015, 2018b; Fogarty and El-Tawil 2016; Wu et al. 2018) studies as well.

As shown in previous studies (Elkady and Lignos 2015, 2018b), such responses can be accurately simulated through Continuum Finite Element (CFE) simulations that are able to explicitly simulate

---

[1] Graduate Research Assistant, Dept. of Civil and Environmental Engineering, Univ. of California, Davis, CA 95616.

[2] Professor, Dept. of Civil and Environmental Engineering, Univ. of California, Davis, CA 95616 (corresponding author). Email: kanvinde@ucdavis.edu

[3] Graduate Research Assistant, Civil Engineering Institute, Ecole Polytechnique Fédérale de Lausanne, Lausanne, CH-1015, Switzerland.

[4] Postdoctoral Scholar, Civil Engineering Institute, Ecole Polytechnique Fédérale de Lausanne, Lausanne, CH-1015, Switzerland.

[5] Associate Professor, Civil Engineering Institute, Ecole Polytechnique Fédérale de Lausanne, Lausanne, CH-1015, Switzerland. ORCID: https://orcid.org/0000-0003-0682-4660

Note. This manuscript was submitted on July 25, 2022; approved on November 30, 2022; published online on March 9, 2023. Discussion period open until August 9, 2023; separate discussions must be submitted for individual papers. This paper is part of the ***Journal of Structural Engineering***, © ASCE, ISSN 0733-9445.

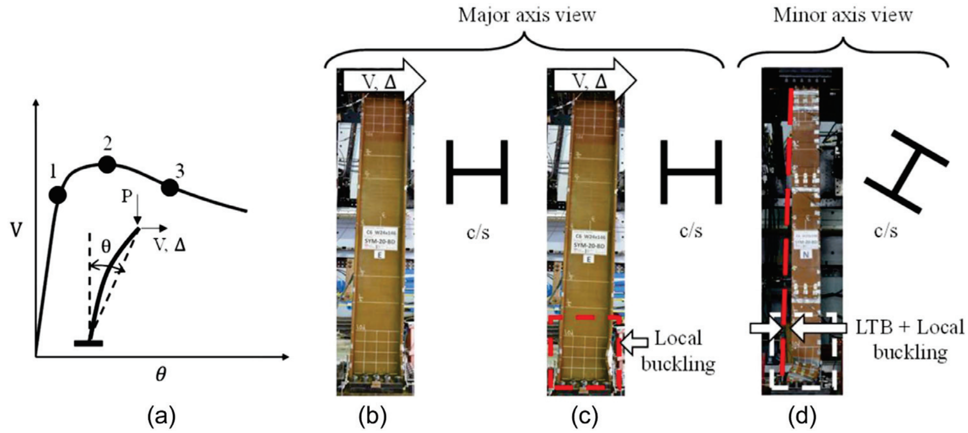

Fig. 1. Representative interactive buckling from experiments (W24X146, $P/P_y = 0.2$): (a) schematic load-deformation curve; deformed states at chord rotation (θ): (b) 2%, (c) 3%, and (d) 4%.

these various phenomena and their interactions. However, these are generally regarded as being prohibitively expensive within the context of structural performance assessment (ASCE 2017; FEMA 2009; PEER/ATC 2010). The structural engineering research and professional practice rely almost exclusively on frame elements; consequently, these are the focus of this paper. Within frame elements, the popular approaches to simulate IB include concentrated hinge or spring type models (Dides and de la Llera 2005; Ibarra et al. 2005), or fiber elements (Kolwankar et al. 2018, 2020; Krishnan 2010; Spacone et al. 1996). However, both of these approaches are inadequate because they (in their common interpretations and implementations) fail to capture the fundamental physics of IB. Specifically, zero length elements cannot capture the spread of plasticity, and typically cannot capture axial force flexure interactions or axial force-flexure-torsion interactions. Moreover, they usually reflect only in-plane response, and do not, in general, simulate the three-dimensional response shown in Fig. 1. Conventional fiber-based elements address some of these limitations (e.g., spread of plasticity and axial-force-moment interactions) but usually do not incorporate cross-sectional warping or the effect of shear strains, both of which are important especially when torsional deformation modes are involved. As a result, these approaches are usually calibrated in an *ad hoc*, phenomenological way to match the load-deformation response of specific experiments. This compromises their generality when extrapolated to new structural configurations or loadings.

Motivated by the above, this paper formulates and implements a displacement-based fiber element that can simulate IB in steel beam-columns. Termed the Torsion Fiber Element (TFE), the element incorporates the following features: (1) a multiaxial fiber construct to represent normal and shear stress interactions at the fiber level and ultimately axial, flexural, shear, and torsional interactions at the cross-sectional level, (2) spread of plasticity and effective softening due to local buckling, (3) consideration of warping as well St. Venant torsion through a 14 degree of freedom element and new deformation interpolation functions, (4) rigorous incorporation of geometric nonlinearities to enable simulation of various forms of buckling and post-buckling response, and (5) complete numerical implementation in the simulation platform OpenSees (version 3.0.0a). The next section provides background, including a summary of relevant work in the area. Following this, observations from CFE simulations conducted as part of this study are presented, along with prior experimental results—these inform the element formulation and also serve as a testbed for the validation of the proposed TFE. The element formulation and implementation are then presented, and results are compared against their counterparts from the CFE simulations and one experiment. The paper concludes by summarizing limitations along with ongoing and future work.

Background and Scope

Numerous studies have experimentally, computationally, and analytically investigated lateral torsional buckling, local buckling, and more recently, IB. These studies establish: (1) a comprehensive understanding of the phenomenology of these response modes, (2) a theoretical understanding of basic attributes such as internal strain distributions (generally under elastic conditions), and (3) mathematical formulations and geometric transformations that enable their representation through frame elements. Early work (Farwell and Galambos 1969; Fukumoto and Galambos 1966; White 1956) on the topic of inelastic lateral torsional buckling of steel beam-columns established a basic understanding of the physical phenomena which, through several refinements (e.g., Subramanian and White 2015) continues to influence current design codes (AISC 2016a, b); Kemp (1996) provides an overview of the important aspects of this seminal body of work. This work is underpinned by theoretical developments (Timoshenko 1945) regarding internal stress/strain fields and deformation modes through which open sections resist combinations of applied flexure, shear, and torsion (uniform and non-uniform). More recent experimental (Newell and Uang 2008; Elkady and Lignos 2018a; Suzuki and Lignos 2021; Cravero et al. 2020; Chansuk et al. 2021) and computational (Elkady and Lignos 2015, 2018b; Fogarty and El-Tawil 2016; Wu et al. 2018) studies provide additional data under seismic loading. In the context of this paper, the main observations from these studies are that: (1) conventional Euler–Bernoulli beam theory, in which plane sections remain plane (PSRP) is utilized, cannot capture the mechanics of warping torsion that are essential to inelastic lateral torsional response of open sections, and (2) the response is controlled by interactions between longitudinal (i.e., axial) and shear stresses, which results in strong coupling between various stress resultants as interpreted at the member ends or cross-sections. Work by Simo and Vu-Quoc (1991), Pi and Trahair (1994a, b) has resulted in frame elements to represent this type of response, albeit the former focuses on elastic response, whereas the latter considers only warping torsion

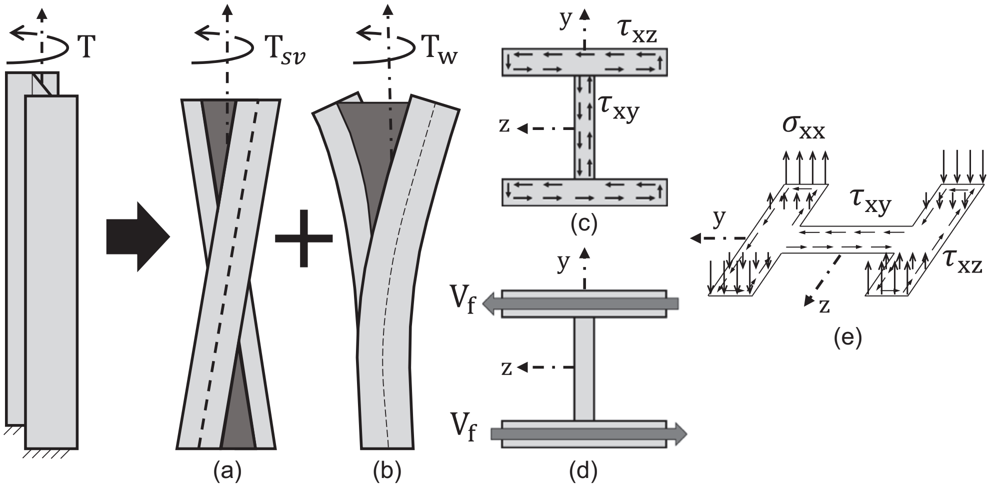

Fig. 2. Mechanism of torsion in I-section: deformation associated with (a) St. Venant's torsion and (b) warping torsion; (c) shear flow due to St. Venant's torsion; (d) shear in flange due to warping torsion; (e) combined state of stress due to applied torsion.

(and neglects shear strains), focusing on thin-walled sections. More recently, Du and Hajjar (2021) developed a nonlinear frame element for single angle and tee sections accounting for inelastic torsion warping. While these various formulations address important aspects of response, they remain application specific and none can account for all the combined effects present in open section members that have significant contributions from St. Venant torsion (i.e., thick-walled sections vis-à-vis PSRP which arises from shear flow around the cross section), as well as warping torsion (which arises from torsion-induced weak-axis bending of the flanges); Figs. 2(a–e) illustrate these phenomena.

These two types of torsion result in interactions between shear and longitudinal strain at the continuum level [Fig. 2(e)], which cannot usually be accommodated into conventional fiber element formulations, and only consider longitudinal local strains. Research by Le Corvec and Filippou (2011) is particularly notable in this regard. This work provides a general framework for the incorporation of cross-sectional warping deformations into a force-based fiber element constructs, and is applied to simulate interactive flexural, shear, and torsional response of beam-columns. This is done through the introduction of an arbitrary number of additional degrees of freedom to interpolate warping deformations. The element formulation presented in this paper may be considered a particularization of the Le Corvec and Filippou (2011) approach, focusing on physically intuitive (and well-established) deformation modes and force resultants, such as twist rate and the bimoment to describe the response of beam-columns. The formulation in this paper is also different insofar as it focuses on displacement-based elements rather than force-based. While the research described above provides the basis for simulating a response at the member scale, it requires additional enrichment to simulate local buckling, which is integral to IB. A common approach for simulating local buckling in fiber elements is to represent it as effective constitutive softening. This approach has been used successfully by several researchers (Hajjar et al. 1998; Kolwankar et al. 2018, 2020). Suzuki and Lignos (2018) developed uniaxial material models specifically to represent local buckling in fiber elements, and other researchers (Kolwankar et al. 2020) have provided means for their calibration and regularization (to mitigate the effects of mesh dependence or non-objectivity). The method presented in this paper uses a similar approach, except that the effective softening material is a multiaxial one, to account for the interactions between shear and longitudinal stresses. This study builds on these previous developments to propose an element formulation with the features described in the Introduction. This formulation is applicable to bisymmetric open sections (specifically, I-beams) and (in its current form) is limited to monotonic loading. Local buckling is represented through an adaptation of a von Mises hardening plasticity model with effective softening. It should be noted that the proposed TFE formulation, along with the use of a softening von Mises material law, aims to simulate element response well past its peak capacity. For applications that require only precise estimates of the member load-bearing capacity, other well calibrated methodologies exist, such as the strain-averaged Continuous Strength Method (Fieber et al. 2019).

Continuum Finite Element Simulations and Experimental Data

Benchmark data for model development and validation was primarily derived from CFE simulations conducted as part of this study, along with a previously conducted physical experiment by Farwell and Galambos (1969). While the experiment provides direct observations of response, the CFE simulations are advantageous for three reasons. First, they simulate the behaviors of interest (i.e., elastoplastic response, local, lateral torsional, and IB) accurately, representing all the relevant physics. Second, they enable the interrogation of a large range of parameters and loading conditions that are challenging to examine in a physical or experimental setting. Finally, they allow for the recovery of deformation fields and internal stress variables at a scale and resolution that are unfeasible to assess in experiments; this is particularly important from the standpoint of formulating the element and the underlying strain interpolations. Referring to Fig. 3(a), each simulation was a single member subjected to a range of boundary conditions and loadings that are summarized in Table 1. Figs. 3(b–c) show the deformed shape of one such simulation (Simulation #18; see Table 1) indicating an IB mode with local buckling as well as lateral torsional buckling. The boundary conditions and loadings shown in Table 1 feature a mix of flexural, torsional, and axial loads applied in various ways and are intended to represent conditions that are present in typical first story columns. The parameter sets include a wide range of flange slenderness [$4 < (b_f/2t_f) < 10$], ranging from highly ductile to moderately ductile as per AISC (2016b), web slenderness [$35 < (h/t_w) < 60$] - a majority being beyond the high

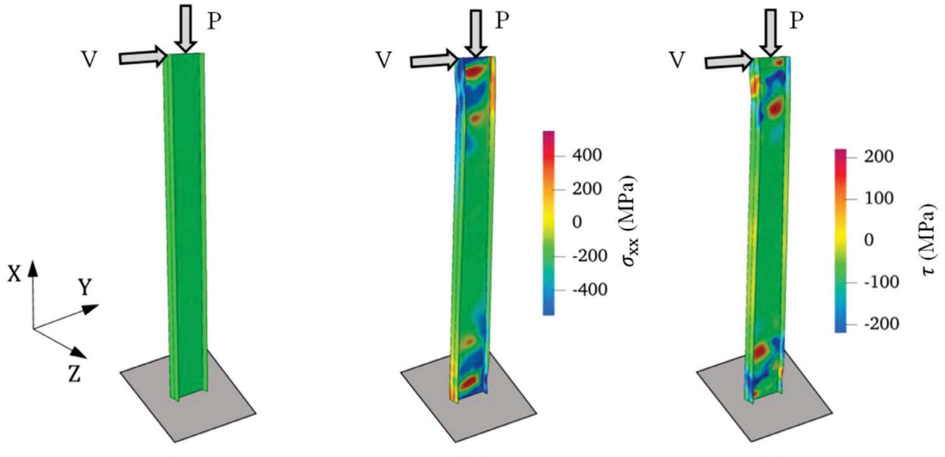

(a) (b) (c)

Fig. 3. Representative continuum finite element (CFE) model (simulation #18): (a) undeformed column; (b) axial stress (σ_{xx}); and (c) in-plane shear stress (τ) distribution at drift level 4%.

Table 1. Investigated Problems (i.e., Simulation matrix) and associated parameters

Sim. number	Load type	Section	$b_f/2t_f$	h/t_w	Length (mm)	Boundary conditions	P/P_y	Observations
1, 2, 3	θ_x[a]	W24X131	6.70	35.6	5,486	TR – Fr[b]	0, 0.2, 0.3	T[c]
4, 5, 6	θ_x	W24X103	4.59	39.2	5,486	TR – Fr	0, 0.2, 0.3	T
7, 8, 9	θ_x	W24X84	5.86	45.9	5,486	TR – Fr	0, 0.2, 0.3	T
10, 11, 12	Δ_y[d]	W24X131	6.70	35.6	5,486	Fx – Fx[e]	0, 0.2, 0.3	IB[f]
13, 14, 15	Δ_y	W24X131	6.70	35.6	5,486	Fx - Fr[g]	0, 0.2, 0.3	LT[c]
16, 17, 18	Δ_y	W24X103	4.59	39.2	5,486	Fx – Fx	0, 0.2, 0.3	IB
19, 20, 21	Δ_y	W24X103	4.59	39.2	5,486	Fx – Fr	0, 0.2, 0.3	LT
22, 23, 24	Δ_y	W24X84	5.86	45.9	5,486	Fx – Fx	0, 0.2, 0.3	IB
25, 26, 27	Δ_y	W24X84	5.86	45.9	5,486	Fx – Fr	0, 0.2, 0.3	LT
28, 29, 30	Δ_y	W24X55	6.94	54.6	5,486	Fx – Fx	0, 0.2, 0.3	LT
31, 32, 33	Δ_y	W21X101	7.68	37.5	5,486	Fx – Fx	0, 0.2, 0.3	IB
34, 35, 36	Δ_y	W21X101	7.68	37.5	5,486	Fx – Fr	0, 0.2, 0.3	LT
37, 38	Δ_y	W21X48	9.47	53.6	5,486	Fx – Fx	0, 0.2	IB

[a] Applied twist (θ_x) (Displacement controlled).
[b] One end strictly torsion restrained, the other end free, both ends warping restrained.
[c] Torsional (T) and lateral torsional (LT) response, together termed as global torsion (GT).
[d] Applied lateral displacement (Δ_y) for major axis bending (Displacement controlled).
[e] One end fixed, the other end with restrained rotations (both ends warping restrained).
[f] interactive buckling (IB) response.
[g] One end fixed; the other end entirely free (both ends warping restrained).

ductility limit as per AISC (2016b), and a wide range of global member slenderness ratios [$50 < (L/r_y) < 150$] – a majority being higher than the plastic LTB slenderness ratio limit of L_p/r_y as per AISC (2016a). Two different types of end conditions are also considered: (1) Fx-Fr: wherein one end is fully restrained and the other (loading end) is fully free except for the minor axis displacement (Δ_z), and (2) Fx-Fx: wherein one end is fully restrained, and the other (loading end) has restrained rotations as well as the minor axis displacement (Δ_z - refer to Table 1); warping is restrained for both the cases. In terms of moment gradient ratio (M:V), the latter is lower than the former with all other conditions being the same. These variables allow for the examination of response in cases where lateral torsional buckling or when local buckling is dominant (i.e., high L/r_y and high moment gradient or low L/r_y and low moment gradient, respectively) – the LTB dominated or pure torsional responses are notated LT in Table 1, or when IB is highly likely (moderately high values of both L/r_y and the moment gradient); these are notated IB. The methodology used for the construction of these CFE models has been exhaustively validated by Elkady and Lignos 2015, 2018b against experimental data (Elkady and Lignos 2018a; Newell and Uang 2008); consequently, such validation is not presented here.

Figs. 3(b and c) show contour plots of the stress components: axial stress σ_{xx} as well as in-plane shear τ in a region of interest near the local buckle; indicating that the material is subjected to a complex stress state composed of both axial as well as shear stresses, neither of which can be disregarded. These simulation models were constructed using the software ABAQUS (2020) using protocols developed by Elkady and Lignos (2015). The members were idealized by shell elements (4 node reduced integration; S4R in ABAQUS), with an element size on the order of 25 mm × 25 mm (small relative to section depths in the range of 500–600 mm, and overall member length in the range of 5,000–6,000 mm) to achieve mesh convergence. Initial imperfections were introduced into the model as perturbations to initiate local buckling. The size and shape of these imperfections are based

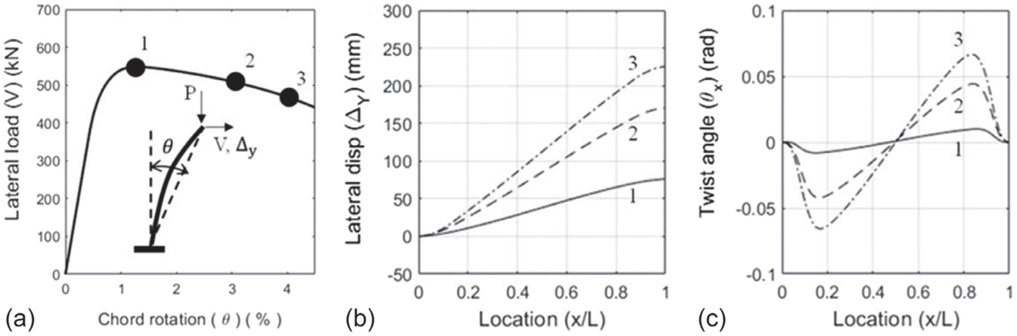

Fig. 4. Results from representative continuum finite element (CFE) model (simulation #18): (a) load-deformation response; (b) lateral displacement profiles; and (c) twist angle profile.

on procedures developed by Elkady and Lignos 2015, 2018b. The material constitutive response was represented through a von Mises yield surface with isotropic-kinematic hardening and one back stress (Lemaitre and Chaboche 1990), with parameters calibrated to represent A992 Grade 50 steel commonly used in United States construction; the parameter values are summarized in Elkady and Lignos 2018b. It is emphasized here that the constitutive material is monotonically hardened, such that all forms of softening (measured at the global scale) occur due to geometric nonlinear effects, such as local or lateral torsional buckling. Residual stresses were not incorporated, either in the CFE simulations or the TFE simulations (presented later) for consistency. The primary information extracted from the CFE simulations (and the experiment) was the load-deformation curves. Additionally, deformations (measured both in terms of continuum strains profiles and displacement variables in three dimensions) was recovered from each of the simulations. Figs. 4(a–c) show a sample of such recovered results, all from Simulation #18, which features W24X103 (Fx-Fx end condition) subjected to an axial load of $0.3P_y$ (constant throughout and applied as a force) followed by a lateral force (applied by an imposed displacement history at the top of the column). Fig. 4(a) shows the lateral load versus chord rotation [see inset of Fig. 4(a)], whereas Figs. 4(b and c) show the distribution of two deformation variables, i.e., the lateral displacement Δ_y and the twist θ_x, over the length of the member, at loading instants 1, 2, and 3 marked in Fig. 4(a). It is noted here that the lateral displacement shown in Fig. 4(b) reflects the displacement of the centerline of the CFE model, whereas the twist is idealized by the rotation of the imaginary line connecting the flange centroids about the member longitudinal axis (x-axis). This facilitates a consistent comparison with the results of the frame element introduced in the next section. Similar results were recovered for all 38 simulations listed in Table 1. In addition to the recovered quantitative data from these simulations, qualitative data (e.g., stress and strain patterns) from these simulations [similar to those indicated in Figs. 3(b and c)] were inspected to develop intuition regarding internal stress and strain distributions.

Element Formulation for the Torsional Fiber Element

The discussion of the element formulation is divided into three subsections. First, the element construct, section kinematics, and deformation interpolations are presented. This is followed by a description of the approach used for the incorporation of geometric nonlinearity, using an updated Lagrangian formulation. The section concludes by describing the numerical implementation.

TFE Construct, Section Kinematics, and Deformation Interpolation

Fig. 5(a) shows the frame element and degrees of freedom. Referring to the figure, the member has 14 degrees of freedom (dofs). Of these, two (i.e., dof u_i and u_j) correspond to axial deformations, eight $(v_i, w_i, \theta_{z_i}, \theta_{y_i}, v_j, w_j, \theta_{z_j}$ and $\theta_{y_j})$ correspond to flexural and shear deformations, whereas four $(\theta_{x_i}, \theta'_{x_i}, \theta_{x_j}$ and $\theta'_{x_j})$ correspond to torsional deformations. Of the torsional dofs, two correspond to the twist angles (θ_{x_i} and θ_{x_j}) at ends i and j, whereas dofs θ'_{x_i} and θ'_{x_j} correspond to the twist rates at these ends. The work-conjugate forces for each of these are straightforward, i.e., the moments for the flexural rotations, axial forces, and shear forces

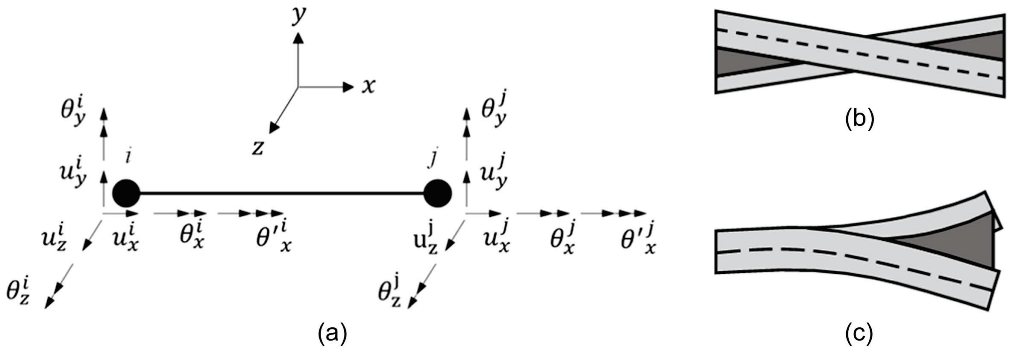

Fig. 5. Proposed TFE construct: (a) TFE element with displacement components; (b) deformation due to St. Venant's torsion; and (c) deformation due to warping torsion.

for the axial and lateral displacements, and the torsional moment for the twist. The work-conjugate force for the twist rate (and/or the warping) is the bimoment. The element construct is similar to the well-established elastic warping torsion element originally proposed by Bathe and Wiener (1983) and described in detail by McGuire et al. (2000). The deformation of each cross section is considered to be a superposition of the following deformations:

u' : strain at centerline
θ_z' : curvature about z-z axis
$-\theta_y'$: curvature about y-y axis
θ_x' : twist rate

Of these, the axial deformation (i.e., centerline stretch) and the flexural deformations (i.e., the curvatures in both directions) carry their usual meanings from the Euler–Bernoulli beam theory (e.g., see Le Corvec 2012). The torsional deformations are schematically illustrated in Figs. 5(b and c). As shown in these figures, the torsional deformations may be decomposed into those that arise from St. Venant torsion (i.e., wherein plane sections remain plane – see Fig. 5(b); in the elastic case this corresponds to the torsional rigidity GJ), and warping torsion. The latter (which corresponds to the torsional constant in the elastic case EC_w, in which C_w is the warping constant of the cross section), for an open I-section (or wide-flanged section), is characterized by the formation of a shear couple due to the bending of each of the flanges in the weak-axis of the cross section that occurs due to torsional deformation of the cross section – see Fig. 5(c). The centerline generalized displacements (u, v, w, and θ_x) at any cross section (i.e., longitudinal location x) are interpolated from the end displacements as described below in Eqs. (1)–(4). As discussed in the next subsection, these displacement interpolations are applied for incremental (rather than total) displacements within an updated Lagrangian framework

$$u(x) = N_{l_1}(x)u_i + N_{l_2}(x)u_j \tag{1}$$

$$v(x) = N_{c_1}(x)v_i + N_{c_2}(x)\theta_{z_i} + N_{c_3}(x)v_j + N_{c_4}(x)\theta_{z_j} \tag{2}$$

$$w(x) = N_{c_1}(x)w_i - N_{c_2}(x)\theta_{y_i} + N_{c_3}(x)w_j - N_{c_4}(x)\theta_{y_j} \tag{3}$$

$$\theta_x(x) = N_{c_1}(x)\theta_{x_i} + N_{c_2}(x)\theta_{x_i}' + N_{c_3}(x)\theta_{x_j} + N_{c_4}(x)\theta_{x_j}' \tag{4}$$

In the above equations, the subscripts i and j represent the two nodes of the member, such that the terms that feature them represent the nodal displacement quantities (e.g., u_i represents the displacement in the x-direction at node i, and so on). The interpolation functions themselves are

$$N_{l_1}(x) = 1 - \frac{x}{L_e}, \qquad N_{l_2}(x) = \frac{x}{L_e} \tag{5}$$

$$N_{c_1}(x) = 1 - 3\left(\frac{x}{L_e}\right)^2 + 2\left(\frac{x}{L_e}\right)^3 \tag{6}$$

$$N_{c_2}(x) = L_e\left(\frac{x}{L_e} - 2\left(\frac{x}{L_e}\right)^2 + \left(\frac{x}{L_e}\right)^3\right) \tag{7}$$

$$N_{c_3}(x) = 3\left(\frac{x}{L_e}\right)^2 - 2\left(\frac{x}{L_e}\right)^3 \tag{8}$$

$$N_{c_4}(x) = L_e\left(-\left(\frac{x}{L_e}\right)^2 + \left(\frac{x}{L_e}\right)^3\right) \tag{9}$$

Referring to Eqs. (5)–(9) above, the axial displacements are interpolated in a linear manner, whereas the flexural and torsional displacements are interpolated with cubic Hermite polynomials. Once the centerline displacements have been interpolated from the nodal displacements, they may be transformed to the continuum displacements through the following relationships

$$u^c(x, y, z) = u(x) - y\theta_z(x) + z\theta_y(x) - \boldsymbol{yz\theta_x'(x)} \tag{10}$$

$$v^c(x, y, z) = v(x) - z\theta_x(x) \tag{11}$$

$$w^c(x, y, z) = w(x) + y\theta_x(x) \tag{12}$$

The above relationships imply a Plane-Parts-Remain-Plane (PPRP) rather than a PSRP condition, such that the "parts" of the section, i.e., the webs and the flanges remain plane individually, but the section as a whole experiences warping deformations. The warping deformations are introduced through the bolded term $\boldsymbol{yz\theta_x'(x)}$ and are determined only for the flanges. The 'z' term in this equation expresses the assumed warping function. Note that the second terms in Eqs. (11) and (12): $z\theta_x(x)$, and $y\theta_x(x)$, are conventionally not included or shown in standard beam formulations, and represent displacements associated with St. Venant torsion; these become relevant only when they are used to compute continuum shear strains, as done in this study. The displacements may then be converted to point-wise strains (over the cross section) so that the constitutive relationship may be invoked at each fiber location to determine the stresses. For the longitudinal strains, this follows well-established kinematic relationships used in conventional fiber elements

$$\varepsilon_{xx}(x, y, z) = u'(x) - y\theta_z'(x) + z\theta_y'(x) - yz\theta_x''(x) \tag{13}$$

Referring to the equation above, the longitudinal strain ε_{xx} may be decomposed into the strains arising from axial stretching u, bending about both axes (y and z), and warping due to torsion (warping dof: θ_x'). The longitudinal strains in the cross-sectional plane (along directions y and z), along with the shear strain in the cross-sectional plane (γ_{yz}), are also assumed to be zero, implying that each cross section retains its original shape without in-plane distortion; this is consistent with experimental and CFE observations. This leaves the shear strains γ_{xy} and γ_{xz}, which produce shear stress on the cross-sectional surface. These shear stresses resist the St. Venant torsion [refer to Fig. 2(b) shown earlier]. However, there is no established way to determine these shear strains from the cross-sectional deformations. Consequently, a strain field is proposed for which the visual interpretation is illustrated in Fig. 6. Referring to this figure, the basic concept is consistent with the manner in which shear stresses are inferred in thin-walled open sections (e.g., see Timoshenko 1945). The underlying assumptions are that: (1) the shear flow is parallel to the long-edge of any part of the section (i.e., web or flange), i.e., γ_{xy} is zero in the flange, and γ_{xz} is zero in the web; (2) the shear strains are zero at the centerline of the web and the flange, and increase linearly outward from there; (3) the shear strains maintain compatibility with the twist rate in a manner as described by Eqs. (14) and (15) below. In the web, the shear strain field $\gamma_{xy}(x, y, z)$ is interpolated as follows [Fig. 6(b)]

$$\gamma_{xy}(x, y, z) = -2\theta_x'(x) \tag{14}$$

In the flanges, the shear strain field $\gamma_{xz}(x, y, z)$ is expressed as follows [Fig. 6(b)]

$$\gamma_{xz}(x, y, z) = -2y_{flange}\theta_x'(x) \tag{15}$$

In the above equation, $y_{flange} = y \mp h/2$, depending on whether the flange in question is located at $+h/2$ or $-h/2$. It is noted here

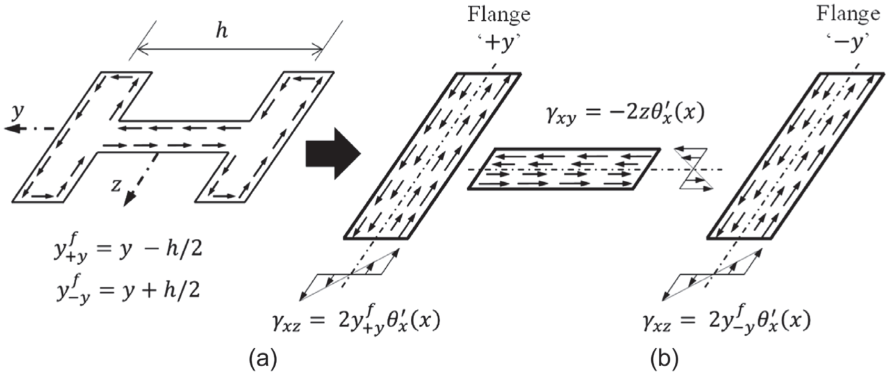

Fig. 6. Shear flow pattern for St. Venant's torsion: (a) actual shear flow in I-section for torsion; and (b) idealized shear flow diagram for torsion.

that the term h here represents the height of the web [measured between the center of the flanges – see Fig. 6(a)], wherein the cross section is idealized as an assembly of three rectangles (one for the web and two for the flanges), and carries a different meaning than the h in the web slenderness ratio h/t_w, wherein it represents the height of the web disregarding the fillet transition to the flange. The strain field may be considered analogous to the Prandtl stress field (see Timoshenko 1945) for thin-walled open sections subjected to torsion. Eqs. (1)–(15) enable the determination of the strains ε_{xx}, γ_{xy}, and γ_{xz} at a fiber location (y, z) and at any longitudinal location x. Note that unlike a conventional fiber element, which has only one component of the fiber strain, i.e., ε_{xx}, the fibers here have three components, including the shears γ_{xy} and γ_{xz}. Incorporation of these shear strains is important from the standpoint of effectively incorporating both warping and St Venant torsion, along with their inelastic response. This is an improvement over conventional fiber elements that usually: (1) disregard warping torsion entirely; and (2) incorporate St Venant torsional response only in an elastic sense, i.e., by prescribing a GJ/L stiffness between the torsional degrees of freedom (e.g., OpenSees version 3.0.0a). Once the fiber level strains have been determined as above, they may be used within any suitable multiaxial constitutive model to estimate the fiber stresses; the selection and calibration of constitutive models in the context of this study is the topic of later discussion. The stresses computed in this manner may then be used for force recovery (or state determination) in conjunction with a formulation of geometrical nonlinearity, within an appropriate solution algorithm for analysis of the structure.

Numerical Implementation and Geometric Nonlinearity

Fig. 7 schematically illustrates the computational implementation of the element. The element formulation is implemented within OpenSees (version 3.0.0a), which has a standard predictor-corrector

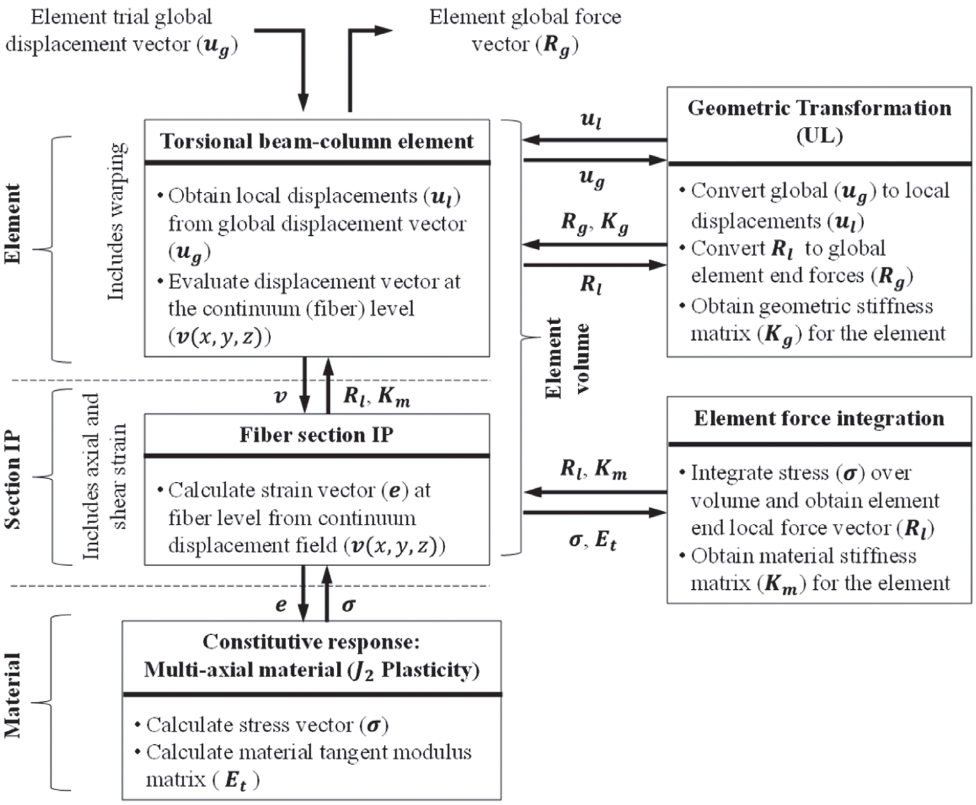

Fig. 7. Flow diagram for force recovery process of TFE with multiaxial material model.

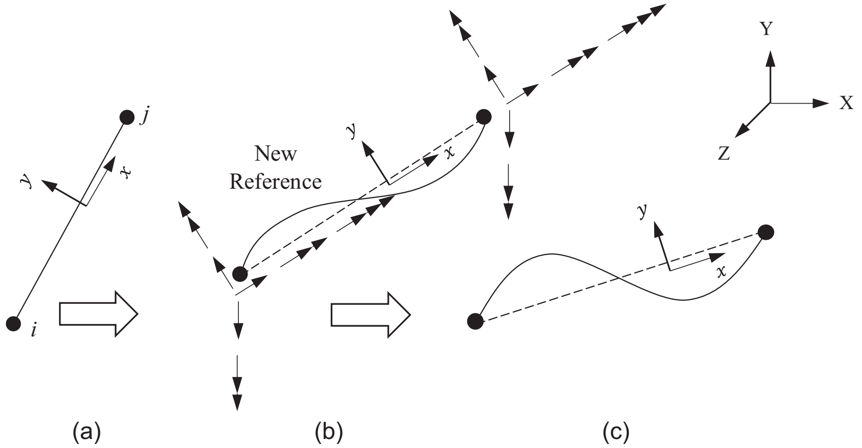

Fig. 8. Updated Lagrangian (UL) reference system in the TFE construct: (a) the initial state and (b)–(c) deformed state.

algorithm for global solution. This algorithm involves estimating trial displacement vectors based on the applied loads and a tangent stiffness, and then obtaining a converged solution by minimizing an appropriate residual. The residual is based on an internal force, which in turn is calculated from the element force recovery or state determination (Yang et al. 2007). During each iteration, the element input from the global solution algorithm is a trial element displacement vector $\boldsymbol{u^g}$ (and a corresponding incremental displacement vector $\boldsymbol{du^g}$) in global coordinates. The output, back to the global solution algorithm is an element force vector $\boldsymbol{P^g_{int}}$, also in global coordinates, in addition to a tangent stiffness matrix ($\boldsymbol{K_T}$) for the element. The former is used to construct the global internal force vector and minimize the residual. All element-level operations are performed in an updated Lagrangian (UL) construct, i.e., using the last converged state of the element as the reference configuration—see Fig. 8.

The first step is to convert the global incremental displacements $\boldsymbol{u^g}$ to local coordinates, and then use the shape functions [Eqs. (5)–(9)] and the transformation Eqs. (13)–(15) to determine the strains ε_{xx}, γ_{xy}, and γ_{xz} at each fiber location (the other strains are assumed zero). Once these are determined, they are passed to the constitutive model, which in this case is a von Mises (J_2) plasticity model available in OpenSees as ‘ J_2 plasticity.’ The fiber level stresses (σ_{xx}, τ_{xy}, and τ_{xz}) are returned to the element, which must then be integrated over the cross section and converted to equivalent nodal forces (i.e., force recovery). This step involves the consideration of geometric nonlinearity and equilibrium in the deformed shape. The goal of force recovery is the determination of the element internal force vector $\boldsymbol{P_{int}}$ in the reference frame corresponding to the last converged state at step I [Fig. 8(b)]. Upon convergence, $\boldsymbol{P_{int}}$ should match (within reasonable tolerance) the external load vector $\boldsymbol{P_{ext}}$

$$\boldsymbol{P_{int}} = \boldsymbol{P_{ext}} \tag{16}$$

The internal force may be determined by equating the external and internal virtual work

$$\delta U_{ext} = \delta U_{int} \tag{17}$$

$$\delta_t \boldsymbol{u} \cdot \boldsymbol{P_{ext}} = \int_{V_t} \boldsymbol{T}_t^{t+\Delta t} : \delta_t^{t+\Delta t} \boldsymbol{\varepsilon}(x, y, z) dV_t \tag{18}$$

where $\boldsymbol{T}_t^{t+\Delta t}$ is the 2nd Piola-Kirchhoff stress tensor and $\delta_t^{t+\Delta t}\boldsymbol{\varepsilon}$ is the virtual Green-Lagrange strain tensor for the time increment from t to $t + \Delta t$ (corresponding to step I and I + 1, respectively); calculated considering the converged shape at time t as the reference configuration (UL) [Fig. 8(b)]. The integration is conducted over the material volume (V_t) referenced to time t. A simplified matrix-vector form of the Eqs. (18) is

$$\delta \boldsymbol{u}^T \boldsymbol{P_{ext}} = \int_v \delta \boldsymbol{\varepsilon}^T \boldsymbol{\sigma} dv \tag{19}$$

where $\boldsymbol{\sigma}$ is the continuum stress vector, $\delta\boldsymbol{\varepsilon}$ is the virtual strain vector corresponding to the virtual nodal displacement vector $\delta\boldsymbol{u}$, and v is the element volume at the last converged step ‘I’. The virtual strain vector may be calculated as

$$\delta \boldsymbol{\varepsilon} = \boldsymbol{B} \delta \boldsymbol{u} \tag{20}$$

where $\boldsymbol{B}$ is a matrix containing derivatives of the displacement interpolation functions and the local coordinates of any continuum point. Using Eqs. (20) and (19), we get

$$\delta \boldsymbol{u}^T \boldsymbol{P_{ext}} = \delta \boldsymbol{u}^T \int_v \boldsymbol{B}^T \boldsymbol{\sigma} dv \tag{21}$$

And hence, the recovered internal force vector becomes

$$\boldsymbol{P_{int}} = \int_v \boldsymbol{B}^T \boldsymbol{\sigma} dv = \boldsymbol{P_{ext}} \tag{22}$$

Therefore, the mapping of nodal virtual displacements to the continuum virtual strain measures (using $\boldsymbol{B}$) is required in a UL construct to determine the recovered force vector. Since the axial strain is considered to be the finite Green-Lagrange strain [Eq. (23)] and the shear strain is calculated from the function proposed in Eqs. (14) and (15), two distinct force recovery procedures (for axial and shear strains) are performed, and the recovered forces are superposed.

Axial Strain

The finite Green-Lagrange axial strain is defined as

$$\varepsilon_{xx}(x, y, z) = \frac{\delta u^c}{\delta x} + \frac{1}{2}\left\{ \left(\frac{\delta u^c}{\delta x}\right)^2 + \left(\frac{\delta v^c}{\delta x}\right)^2 + \left(\frac{\delta w^c}{\delta x}\right)^2 \right\} \tag{23}$$

Disregarding $(\delta u^c/\delta x)^2$, since $(\delta u^c/\delta x)^2 \ll (\delta u^c/\delta x)$, and using Eqs. (10)–(12)

$$\varepsilon_{xx}(x,y,z) = \{u' - y\theta_z' + z\theta_y'\} - yz\theta_x'' + \frac{1}{2}\{v'^2 + w'^2\} + \frac{1}{2}\{y^2 + z^2\}\theta_x'^2 + \{yw' - zv'\}\theta_x' \tag{24}$$

Note that the terms $(u' - y\theta_z' + z\theta_y')$ represent the 'linear' strain measure which is already incorporated in a displacement-based beam-column element in OpenSees.

However, the remainder of the "nonlinear" terms introduce several interactions in the element, listed as follows: $\boldsymbol{yz\theta_x''}$ = torsion warping term (only in the flanges); $(\mathbf{1/2})\{\boldsymbol{v'^2 + w'^2}\}$ = axial force–bending interaction; $(\mathbf{1/2})\{\boldsymbol{y^2 + z^2}\}\boldsymbol{\theta_x'^2}$ = Wagner term (axial strain torsion interaction); $\{\boldsymbol{yw' - zv'}\}\boldsymbol{\theta_x'}$ = bending–torsion interaction.

In compact form, the axial strain is represented by the following matrix equation

$$\varepsilon_{xx} = \boldsymbol{Yd} \tag{25}$$

where

$$\boldsymbol{Y} = [\,1 \quad z \quad -y \quad -yz \quad y^2+z^2\,] \tag{26}$$

$$\boldsymbol{d} = \begin{bmatrix} u' + \dfrac{1}{2}(v'^2 + w'^2) \\ \theta_y' - v'\theta_x' \\ \theta_z' - w'\theta_x' \\ \theta_x'' \\ \dfrac{1}{2}\theta_x'^2 \end{bmatrix} \tag{27}$$

The virtual strain becomes

$$\delta\varepsilon_{xx} = \boldsymbol{Y}\delta\boldsymbol{d} \tag{28}$$

Using variational calculus

$$\delta\boldsymbol{d} = \begin{bmatrix} \delta u' + v'\delta v' + w'\delta w' \\ \delta\theta_y' - \theta_x'\delta v' - v'\delta\theta_x' \\ \delta\theta_z' - \theta_x'\delta w' - w'\delta\theta_x' \\ \delta\theta_x'' \\ \theta_x'\delta\theta_x' \end{bmatrix} = \boldsymbol{N}_1\delta\boldsymbol{v} \tag{29}$$

where

$$\boldsymbol{N_1} = \begin{bmatrix} 1 & v' & w' & 0 & 0 & 0 & 0 \\ 0 & -\theta_x' & 0 & 1 & 0 & -v' & 0 \\ 0 & 0 & -\theta_x' & 0 & 1 & -w' & 0 \\ 0 & 0 & 0 & 0 & 0 & 0 & 1 \\ 0 & 0 & 0 & 0 & 0 & \theta_x' & 0 \end{bmatrix} \tag{30}$$

and

$$\delta\boldsymbol{v} = \{\delta u', \delta v', \delta w', \delta\theta_y', \delta\theta_z', \delta\theta_x', \delta\theta_x''\}^T = \boldsymbol{N}_2\delta\boldsymbol{u} \tag{31}$$

where $\delta\boldsymbol{u}$ is the element end virtual displacement vector (14 DOFs) along the **local directions** for the finite element formulation

$$\delta\boldsymbol{u} = \{\delta u_i, \delta v_i, \delta w_i, \delta\theta x_i, \delta\theta y_i, \delta\theta z_i, \delta\theta_{x_i}', \delta u_j, \delta v_j, \delta w_j, \delta\theta_{x_j}, \delta\theta_{y_j}, \delta\theta_{z_j}, \delta\theta_{x_j}'\} \tag{32}$$

and

$$\boldsymbol{N_2} = \begin{bmatrix} N_{l_1}' & 0 & 0 & 0 & 0 & 0 & 0 & N_{l_2}' & 0 & 0 & 0 & 0 & 0 & 0 \\ 0 & N_{c_1}' & 0 & 0 & 0 & N_{c_2}' & 0 & 0 & N_{c_3}' & 0 & 0 & 0 & N_{c_4}' & 0 \\ 0 & 0 & N_{c_1}' & 0 & -N_{c_2}' & 0 & 0 & 0 & 0 & N_{c_3}' & 0 & -N_{c_4}' & 0 & 0 \\ 0 & 0 & -N_{c_1}'' & 0 & N_{c_2}'' & 0 & 0 & 0 & 0 & -N_{c_3}'' & 0 & N_{c_4}'' & 0 & 0 \\ 0 & N_{c_1}'' & 0 & 0 & 0 & N_{c_2}'' & 0 & 0 & N_{c_3}'' & 0 & 0 & 0 & N_{c_4}'' & 0 \\ 0 & 0 & 0 & N_{c_1}' & 0 & 0 & N_{c_2}' & 0 & 0 & 0 & N_{c_3}' & 0 & 0 & N_{c4}' \\ 0 & 0 & 0 & N_{c_1}'' & 0 & 0 & N_{c_2}'' & 0 & 0 & 0 & N_{c_3}'' & 0 & 0 & N_{c_4}'' \end{bmatrix} \tag{33}$$

Therefore, Eq. (28) may be written as

$$\delta\varepsilon_{xx} = \boldsymbol{Y}\delta\boldsymbol{d} = \boldsymbol{YN_1}\delta\boldsymbol{v} = \boldsymbol{YN_1N_2}\delta\boldsymbol{u} = \boldsymbol{B_{axial}}\delta\boldsymbol{u} \tag{34}$$

This equation may be compared to the general Eq. (20). Therefore, using Eq. (22), the recovered internal force vector (14 × 1) due to the axial strain is determined as

$$\boldsymbol{P_{int}^{axial}} = \int_v \boldsymbol{B_{axial}^T}\sigma_{xx}dv = \int_v \boldsymbol{N}_2^T\boldsymbol{N}_1^T\boldsymbol{Y}^T\sigma_{xx}dv \tag{35}$$

wherein the axial stress σ_{xx} is obtained from the strain ε_{xx} using the constitutive model.

Shear Strain

The shear strains from Eqs. (14) and (15) may be written in a compact form as

$$\gamma_{xy}(x,y,z) = -2zH(y - y_2)\{1 - H(y - y_1)\}\theta_x'(x) = k_{t1}\theta_x'(x) \tag{36}$$

$$\gamma_{xz}(x,y,z) = 2y_{+y}^{f}H(y - y_1)\theta_x'(x) + 2y_{-y}^{f}\{1 - H(y - y_2)\}\theta_x'(x) = k_{t2}\theta_x'(x) \tag{37}$$

where $y_1 = [(d/2) - t_f]$ and $y_2 = -[(d/2) - t_f]$, t_f is the flange thickness (y_1 and y_2 are the y-coordinates of the inner-most points of the '$+y$' and '$-y$' flange, respectively), and d is the section depth. θ_x' is the twist rate. The Heaviside function $H(x)$ is defined as

$$H(x) = \begin{cases} 1, & x \geq 0 \\ 0, & x < 0 \end{cases} \tag{38}$$

Eqs. (36) and (37) may be written in matrix form as

$$\begin{bmatrix} \gamma_{xy} \\ \gamma_{xz} \end{bmatrix} = \begin{bmatrix} K_{t1} \\ K_{t2} \end{bmatrix} \theta_x'(x) \tag{39}$$

Now, recalling the Hermite interpolation for twist angles

$$\begin{bmatrix} \gamma_{xy} \\ \gamma_{xz} \end{bmatrix} = \begin{bmatrix} K_{t_1} N_{c_1}' & K_{t_1} N_{c_2}' & K_{t_1} N_{c_3}' & K_{t_1} N_{c_4}' \\ K_{t_2} N_{c_1}' & K_{t_2} N_{c_2}' & K_{t_2} N_{c_3}' & K_{t_2} N_{c_4}' \end{bmatrix} \begin{bmatrix} \theta_{x_i} \\ \theta_{x_i}' \\ \theta_{x_j} \\ \theta_{x_j}' \end{bmatrix} \tag{40}$$

In compact form

$$\boldsymbol{\gamma} = \boldsymbol{B_{shear}} \boldsymbol{\phi_{shear}} \tag{41}$$

where $\boldsymbol{\phi_{shear}} = \{\theta_{x_i}, \theta_{x_i}', \theta_{x_j}, \theta_{x_j}'\}^T$ is the nodal twist displacement. Therefore, the virtual shear strain may be written as

$$\delta\boldsymbol{\gamma} = \boldsymbol{B_{shear}} \delta\boldsymbol{\phi_{shear}} \tag{42}$$

Using Eq. (22), we recover the force vector (torsion and bimoment) for the shear strain vector

$$\tilde{\boldsymbol{P}}_{\boldsymbol{int}}^{\boldsymbol{shear}} = \int_v \boldsymbol{B}_{\boldsymbol{shear}}^T \boldsymbol{\tau} dv \tag{43}$$

The shear stress vector $\boldsymbol{\tau}$ is obtained from the shear strain $\boldsymbol{\gamma}$ using constitutive model J_2 plasticity, where $\tilde{\boldsymbol{P}}_{\boldsymbol{int}}^{\boldsymbol{shear}} = \{M_{x_i}, B_{x_i}, M_{x_j}, B_{x_j}\}_{shear}^T$ gives the nodal torsional moments and bi-moments for the element only for the torsional shear. This force vector can be written for the developed element with 14 DOFs, introducing zero forces for non-torsional degrees of freedom

$$\boldsymbol{P}_{\boldsymbol{int}}^{\boldsymbol{shear}} = \{0,0,0,M_{x_i},0,0,B_{x_i},0,0,0,M_{x_j},0,0,B_{x_j}\}_{shear}^T \tag{44}$$

Superposing Eqs. (35) and (44), the final recovered force vector (14×1 is)

$$\boldsymbol{P_{int}} = \boldsymbol{P}_{\boldsymbol{int}}^{\boldsymbol{axial}} + \boldsymbol{P}_{\boldsymbol{int}}^{\boldsymbol{shear}} \tag{45}$$

The forces $\boldsymbol{P_{int}}$ determined as above reflects the nodal forces in the element as determined in the local configuration corresponding to the trial displacements, i.e., at the '$\mathrm{I}+1$'th step. These are subsequently transformed into global coordinates for residual force ($\boldsymbol{R}$) determination

$$\boldsymbol{R} = \boldsymbol{P}_{\boldsymbol{ext}}^{\boldsymbol{g}} - \boldsymbol{P}_{\boldsymbol{int}}^{\boldsymbol{g}} \tag{46}$$

where $\boldsymbol{P}_{\boldsymbol{ext}}^{\boldsymbol{g}}$ is the external force vector in global coordinates. If the residual tolerance is not met, then a new trial displacement vector is generated, depending on the type of solution algorithm being used (e.g., Newton Raphson), and the process illustrated in Fig. 7 is repeated. When an acceptably small residual is obtained, the structural (and the element) states are assumed to be converged, and the next loading increment is applied. As discussed above, an important output from the element to the global algorithm is the element tangent stiffness; this is assembled into the global stiffness matrix to compute the next trial displacement vector. For the element proposed in this paper, determination of the tangent stiffness matrix also follows a process similar to that for force recovery. Specifically, the j-th column of the tangent stiffness ($\boldsymbol{K_T}$) may be interpreted as

$$\boldsymbol{F^j} = \int_v \boldsymbol{B^T} d\bar{\boldsymbol{\sigma}} dv = \int_v \boldsymbol{B^T D} d\bar{\boldsymbol{\varepsilon}} dv \tag{47}$$

In the above equation, $\boldsymbol{F^j}$ are the incremental (infinitesimal) forces corresponding the infinitesimal strain $d\bar{\boldsymbol{\varepsilon}}$ resulting from incremental infinitesimal displacements $d\bar{\boldsymbol{u}}^{\boldsymbol{j}}$ such that

$$d\bar{\boldsymbol{u}}_i^{\boldsymbol{j}} = \begin{cases} 1, & i = j \\ 0, & i \neq j \end{cases} \tag{48}$$

Matrix $\boldsymbol{D}$ is the material tangent stiffness (at the current step) associated with a continuum point, which is implemented in the J_2 plasticity subroutine within OpenSees. Consequently, each term in the tangent stiffness becomes $\boldsymbol{K}_{\boldsymbol{T}_{ij}}$ and may be determined as

$$\boldsymbol{K}_{\boldsymbol{T}_{ij}} = \boldsymbol{F}_i^{\boldsymbol{j}} \tag{49}$$

One more important output from the solution convergence is the updated geometric state of the element, which becomes the new reference for the next step (UL). The new local axes system is obtained with appropriate 3d rotation matrices (Felippa 2000; McGuire et al. 2000), considering a finite rotation increment between step I and $\mathrm{I}+1$. A new set of the transformation matrices are also evaluated based on the updated local axes used for the global to local displacement (and force) transformation in the next step (Fig. 7). As discussed previously and illustrated in Fig. 7, this entire formulation was implemented within OpenSees (version 3.0.0a), where it was tested to examine its performance for various element definitions as well as loading conditions.

Results and Discussion

Each of the simulations summarized in Table 1 was also conducted using the TFE element. Additionally, an experiment by Farwell and Galambos (1969) was also simulated. The TFE models were subjected to loading and boundary conditions that were identical to their CFE (or the experimental) counterparts. The results are presented in three subsections: (1) a comparison of the TFE model to the experiment by Farwell and Galambos (1969), (2) comparisons of the TFE models to CFE model configurations notated GT (see Table 1, footnote c), i.e., moderate to high member slenderness ratios ($L/r_y > 70$) with free end unrestrained (Fx-Fr); these configurations are susceptible to global torsional modes including lateral and lateral torsional buckling, and are not susceptible to local buckling, and (3) comparisons to CFE models notated IB, that have moderate to high cross-sectional slenderness ($4 < b/2t_f < 10$) and restrained ends (Fx-Fx) and are sensitive to local buckling which then triggers lateral torsional buckling, i.e., interactive buckling (IB – see Table 1, footnote f). It is acknowledged that depending on the parameters, the behavior can gradually transition from one response mode (e.g., GT) to another (e.g., IB). However, organization of the results in the aforesaid manner allows for rigorous examination of the TFE element in each separate context.

Simulation of Experiment by Farwell and Galambos (1969)

Fig. 9(a) schematically illustrates the test setup, boundary conditions, and the loading applied to the experimental specimen by

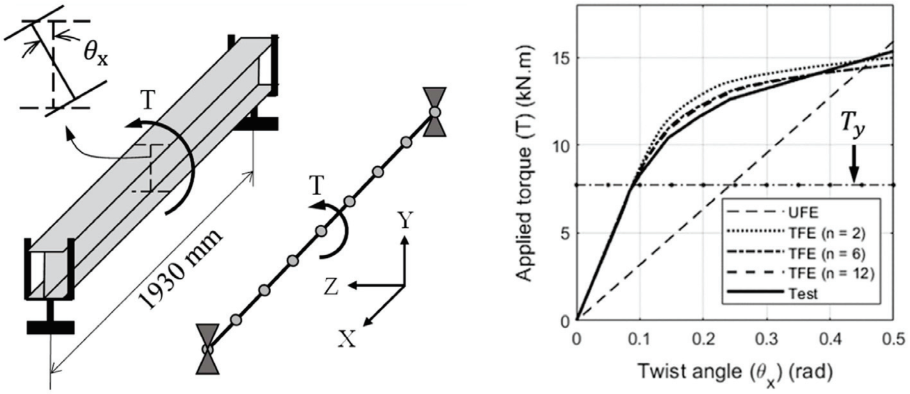

(a) (b) (c)

Fig. 9. Comparison of experimental and TFE simulation results with W6X25 beam: (a) schematic experiment setup; (b) schematic TFE discretization and loading; and (c) comparison of load-deformation plots between test and TFE simulations with different discretization.

Farwell and Galambos (1969). Referring to the figure, the experiment consisted of a simply supported beam (W6X25) loaded with a torsional moment in the center. The end supports restrain the beam against torsional and translational motion in any direction, but not against flexural rotation or warping. The torsional loading was applied in the form of displacement (rotation) control at the center. The key quantities recovered were the load and load-line displacement, which are plotted in Fig. 9(c). Also shown on the figure is the expected yield torsion (T_y) calculated per AISC (1997). As such, the experiment provides the opportunity for baseline validation of the proposed TFE element for torsional loading. A model with the identical physical configuration and boundary conditions was constructed using TFE elements; this model is schematically illustrated in Fig. 9(b). A variable number of elements (n) were considered in the TFE model to examine the efficacy of the TFE formulation. The material constitutive model used for the TFE formulation was the von Mises plasticity model (J_2 plasticity in OpenSees) calibrated to the properties of A36 steel (used in the experiment). The uniaxial stress–strain behavior was idealized as bilinear hardening, with an initial elastic modulus E = 213,000 MPa and shear modulus G = 80,000 MPa; yield stress $\sigma_Y = 285$ MPa; and a post yield stiffness ratio of 3% (Pi and Trahair 1995). The flanges are discretized into 20 fibers along its width, and the web is also discretized into 20 fibers along its depth. Both the flanges and the web are discretized into six fibers through their thickness. This level of discretization may be considered very fine in a conventional fiber-based element. However, in the context of the multiaxial fiber-based model, this finer discretization is necessary to capture the shear strain distribution across the thickness of the web and flanges (Fig. 6). A midpoint integration rule is adopted for the integration over the cross section. A 5-point Gauss–Legendre quadrature rule was adopted for numerical integration along the length (a built-in capability of OpenSees), following Kolwankar et al. (2018, 2020). Fig. 9(c) also overlays the results of the load displacement curve from the TFE model and one uniaxial fiber element (UFE) model (with 12 elements) on the experimental data. Referring to Fig. 9(c), it is evident that when sufficiently refined (see note later) the TFE model is able to capture the load-deformation response up to a fairly large value of rotation (0.5 radians), including the initial elastic slope and hardening, while the UFE model is able to reflect only linear elastic response based on the prescribed GJ value, and does not incorporate warping torsion, and is unable to capture inelastic torsional response. At about 0.5 radians, there is a slight deviation from the experimental data, due to the very high distortion that occurs in the experiment. For context, this twist (beyond which this deviation is observed) is significantly higher than values (~0.2 radians) of practical interest. The mesh refinement study indicates that: (1) the model is mesh-convergent, and (2) when the element length is less than or equal to three times the flange width, the load-deformation results from the TFE models match the experimental data well.

Simulation of Configurations Sensitive to Global Torsional (GT) Modes

Referring to Table 1, 15 out of the 38 CFE simulations listed in Table 1 may be considered sensitive to global torsional modes including torsion or lateral torsional buckling, but not local buckling—these are identified in the table as either LT or T. This is because their global slenderness $\lambda = L/r_y$ is fairly large ($\lambda > \lambda_P^{LTB}$), and this has been associated with a tendency for lateral torsional buckling. From above, λ_P^{LTB} is the member slenderness ratio corresponding to the plastic lateral torsional buckling length (L_p) and defined as

$$\lambda_P^{LTB} = \frac{L_p}{r_y} = 1.76\sqrt{\frac{E}{F_y}} = 42 \tag{50}$$

On the other hand, the flange slenderness ratio is distributed over the "highly ductile" ($\lambda_{HD}^f = 7.35$) and "moderately ductile" ($\lambda_{HD}^f = 9.19$) range, while the web slenderness is beyond the "highly ductile" limit ($\lambda_{HD}^w = 36.05$) as per AISC 341-16 (2016) (Fig. 11). These are of particular interest, because in theory, the proposed element seeks to directly simulate all relevant phenomena (torsion warping, geometric nonlinearity, inelasticity) associated with this type of behavior. Models with TFE elements [similar to that shown in Fig. 9(a)] are constructed complementary to each of these CFE simulations, with identical boundary conditions and loading. For the purposes of demonstration of model results for this set of simulation data, Fig. 10(a) shows the TFE model, whereas Fig. 10(b) shows the undeformed CFE model for simulation #14 (whose parameters are in Table 1). Referring to Fig. 10(a), 38 elements were used to simulate the beam-column; this results in mesh-convergent solutions. This relatively fine mesh is necessitated by the following:

- Interactive modes of buckling with out-of-plane action result in complex deformation fields both longitudinally and over the

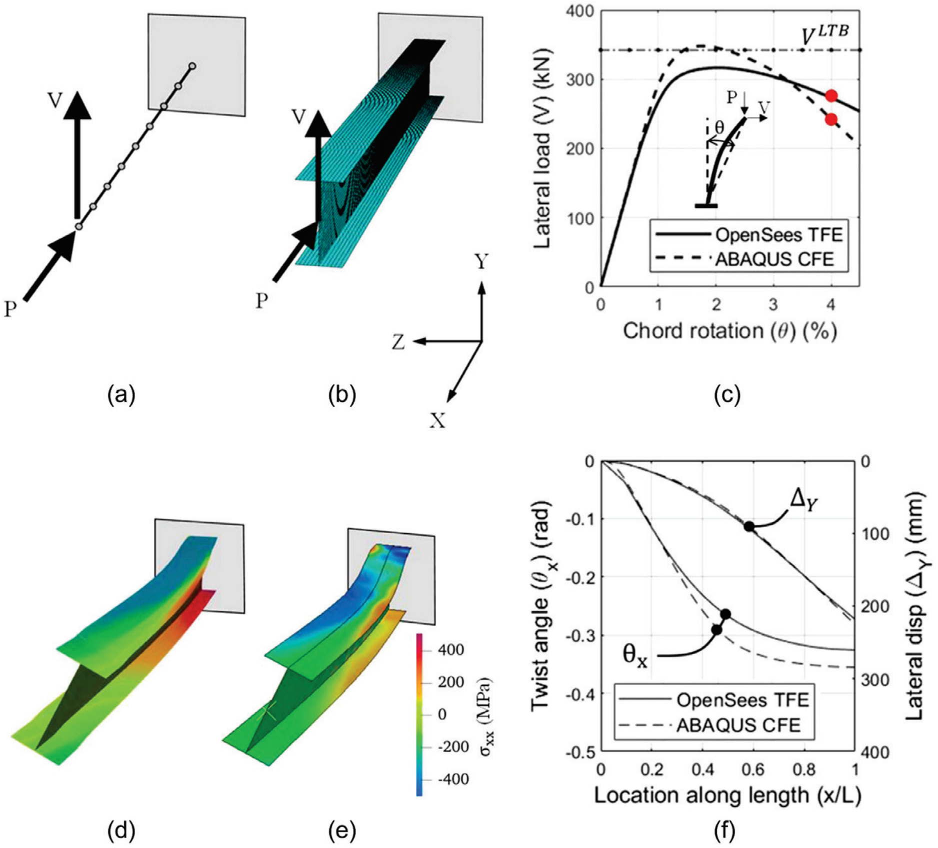

Fig. 10. Comparison between CFE and TFE model results for simulation #14 – W24X13, $P/P_y = 0.2$, Fx-Fr end conditions: (a) TFE model; (b) CFE model (undeformed); and (c) comparison of load-deformation curves; (d) deformation profile and σ_{xx} contours from TFE simulation; (e) deformation profile and σ_{xx} contours from CFE simulation; (f) longitudinal distribution of lateral displacement (Δ_y) and twist angle (θ_x) at the instance shown in the load-deformation curves (4% chord rotation).

cross section; a larger number of elements is necessary to resolve these fields.

- The local coordinate axes of the element are defined based on the current node locations. As large deformations occur between the nodes, these local axes represent only approximately the orientation, which has important implications for the simulation of geometric nonlinearity.
- A key objective of this study is to obtain a deformed shape over the member length to identify the buckling mode along with strain/stress distribution over the entire member. A finer mesh enables a more accurate visualization of these results.

The material used was a multiaxial von Mises plasticity model with combined isotropic-kinematic hardening, implemented in OpenSees as the J_2 plasticity model. The parameters of the model were calibrated as follows: bulk modulus, $\mathrm{B} = 167$ GPa, shear modulus, $\mathrm{G} = 77$ GPa, elastic modulus, $E = 200$ GPa, yield strength (σ_y) and saturation stress (σ_{inf}) of 345 MPa and 450 MPa respectively, post yield linear hardening modulus $H = 3.4$ GPa, and exponential hardening parameter of $b = 12$. These parameters were selected to produce a reasonable match with the material model in ABAQUS (which was calibrated, as discussed earlier, based on guidelines provided by Elkady and Lignos 2018b). Although both constitutive models (ABAQUS as well as OpenSees) are functionally identical, there are minor differences in the way in which they are parameterized, with the implication that an identical set of parameters cannot be used for the two; rather a mapping between parameters is required. Note that because local buckling is not observed in any of these CFE simulations, a monotonically hardening model at the material level is adequate to simulate this response in the frame element-based model as well. Imperfections are however provided in the CFE (following Elkady and Lignos 2018b) as well as TFE models (with global buckling imperfections). Fig. 10(b) shows the undeformed mesh of the CFE model. Fig. 10(c) shows the lateral load-chord rotation curves obtained from both the TFE and the CFE models. Fig. 10(d) shows a deformation profile recovered from the TFE model at the loading instant indicated in Fig. 10(c). Note that the TFE element itself is a one-dimensional entity (i.e., linear), such that the element output is only at the nodes, which cannot be visualized in three dimensions. However, these nodal quantities may be processed to determine internal stresses as well as the implied deformations of the flanges and web through the transformations presented earlier in Eqs. (10)–(12). To visualize these computed quantities (and compare them with their CFE counterparts), a postprocessing module was developed in Visualization Toolkit (VTK) language, which displays these deformations and any field variable of interest (e.g., stress component) on the member webs and flanges. Fig. 10(d) (and all subsequent figures where TFE results are visualized) use this module. Fig. 10(d) may be directly compared to Fig. 10(e), which shows the counterpart results from the CFE simulations. Finally, Fig. 10(f) plots the longitudinal distribution of the angle of twist θ_x as well as the lateral deflection Δ_y as computed from both the CFE and TFE models. Referring to Figs. 10(a–f), the following observations may be made:

1. The load-deformation curve in Fig. 10(c) shows reasonable agreement between the TFE and CFE models; the CFE model

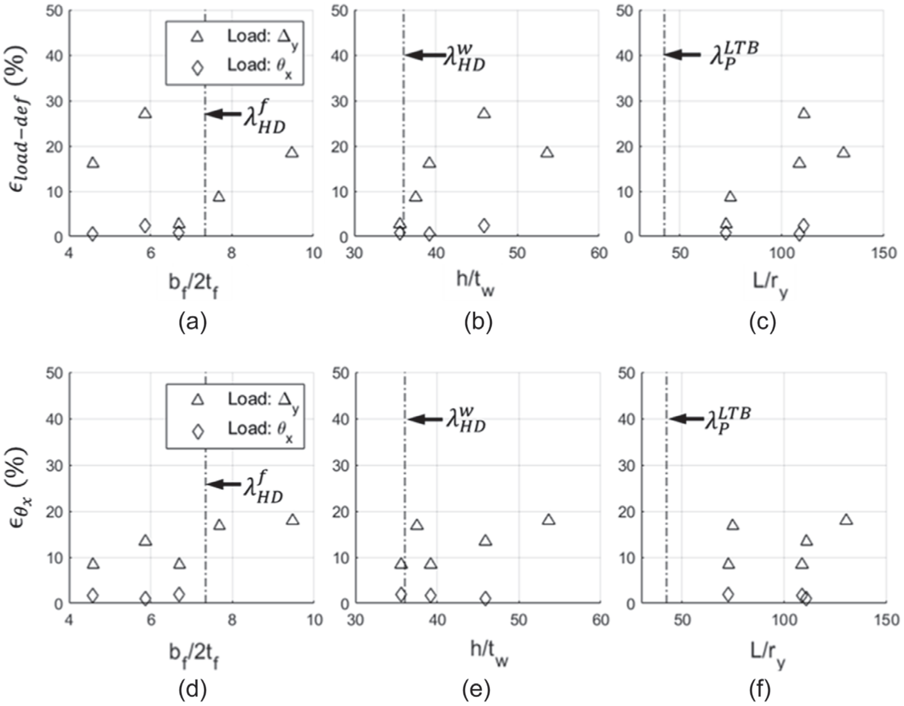

Fig. 11. Measured errors vs section and member slenderness ratio plots for GT response cases: (a)–(c) error in load-deformation; and (d)–(f) error in angle of twist (θ_x)

tends to drop off at a steeper slope as compared to the TFE model. This may be attributed to excessive twist and distortion in the section. Also plotted on the load-deformation curve is the expected inelastic lateral torsional buckling strength (V^{LTB}) determined as per AISC 2016a; referring to the figure, the CFE model predicts this lateral strength accurately whereas the TFE model slightly (~7%) underestimates it. This deviation in ultimate load may be attributed to two factors: (1) The difference hardening rules in CFE and TFE models – specifically, the CFE simulations utilize a von Mises (i.e., J_2) model combined isotropic-kinematic hardening, whereas the TFE assumes a simplified J_2 plasticity model which only incorporates isotropic hardening with some additional linear hardening modulus (a standard ~2% linear hardening modulus is used, in addition to the exponential rule governing the growth of the yield surface (Kolwankar et al. 2018; Pi and Trahair 1995), and (2) the CFE represents geometrically exact nonlinear transformations individually for the flanges and web, whereas in the case of TFE, an idealized UL geometric transformation is adopted. Considering these simplifications, the TFE model represents the response with reasonable (if not ideal) accuracy.

2. The longitudinal distribution of both the transverse deflection and the twist [Fig. 10(f)] appears to be fairly similar between the two. Note here that the transverse drift of the CFE model represents the deflection of the web centerline of the CFE model, whereas the twist of the CFE model is calculated by considering the rotation of the imaginary straight line connecting the centroid of the flanges.
3. The qualitative comparison of the deformed shapes and the stress fields between Figs. 10(d and e) indicate that the TFE model can simulate the spatial distribution of deformations and stresses in a reasonable manner.

Collectively, the above three observations suggest that the TFE model captures the fundamental physics of inelastic lateral torsional response with geometric nonlinearity. It is furthermore noted that the TFE simulations require roughly $1/5^{\text{th}}$ the time as CFE simulations on a standard capacity computer, in addition to requiring only a fraction of the memory. The representative comparisons shown in Figs. 10(a–f) are only for a single configuration, and it is not possible to show similar comparisons for all configurations. Consequently, error measures are generated that can be assessed across the full range of simulations. For the global torsion (GT) configurations (LT along with simulation #1-9 with applied torsion, see Table 1), two error measures are recovered. The first, termed $\epsilon_{load-def}$ is the average relative error between the CFE and TFE load-deformation curves, defined as

$$\epsilon_{load-def} = \frac{\int_0^L (V^{CFE} - V^{TFE}) d\Delta_y}{\int_0^L V^{CFE} d\Delta_y} \times 100\% \tag{51}$$

V^{CFE} and V^{TFE} represent the applied shear in the TFE and CFE models, respectively [Figs. 10(a and b)]. The error is evaluated over the entire loading (until chord rotation of 4.5%). Error measures ϵ_{θ_x} are similarly developed to characterize the agreement between the longitudinal distribution of the twist θ_x. These are defined in a manner similar to $\epsilon_{load-def}$, except that: (1) instead of integrating over the length of the member, they are calculated as the ratio of the maximum twist angle (θ_x) for the CFE and the TFE simulations, and (2) they are evaluated at only a specific instant of loading—corresponding to 4% chord rotation (for LT) or 0.2 rad of applied twist (for torsional loading cases – T)—at which the torsional response has been fully developed. Figs. 11(a–c) plot these three error measures against $b_f/2t_f$, h/t_w, and L/r_y, respectively, to examine the ability of the model to predict the response against key cross-sectional and member variables. Within each figure, the configurations subjected to torsion versus flexure are distinguished. Referring to these figures, it is observed that:

- The error in load-deformation with respect to the member global slenderness ratio L/r_y, is reasonable (<30% in all cases) considering that these situations feature high lateral instability complex twisting modes. Even though flange slenderness $b_f/2t_f$ does not significantly influence error, the error increases with increasing web slenderness h/t_w. Besides, capacity-designed steel MRF columns typically feature an L/r_y lower than 100 (Kircher et al. 2010).

- The error in twist angle ϵ_{θ_x} is in a similar range, suggesting that they are rather insensitive to slenderness ratio, as long as they can initiate the lateral torsional response.
- The cases with torsional loadings (Simulations #1–9) show negligible error in either of the error measures. This is consistent with observations for the experimental results (Fig. 9) by Farwell and Galambos (1969).

Simulation of Configurations Sensitive to Interactive Buckling (IB) Modes

The configurations notated "IB" in Table 1 have similar slenderness ratios as the "LT" cases, implying that they are in the highly and moderately ductile range for flanges and beyond highly ductile ranges for the web of members as per AISC 341-16. However in most of cases, due to the end rotation constraints at the free end ('Fx-Fx' in Table 1), which decreases the moment gradient (M:V), these are susceptible to local buckling, which results in loss of torsional fixity and triggers a torsional mode such as lateral torsional buckling. A key distinction between these and the LT configurations is that in the IB configurations, local buckling results in an effective softening when interpreted at the fiber or cross-sectional level, even if the continuum material hardens monotonically; this is well documented in literature (Hajjar et al. 1998; Kolwankar et al. 2018). As shown previously by Elkady and Lignos (2018b) and Kolwankar et al. (2018), the CFE simulations (with a hardening material law) are able to effectively trace this type of response because they directly simulate the flange and web local buckling phenomena. However, within the construct of the TFE element, this type of response must be represented as effective constitutive softening, because local buckling is not explicitly modeled. Recent work by Kolwankar et al. (2018) and Suzuki and Lignos (2018) has provided insights into this type of constitutive softening, and also provided guidance to calibrate material models to represent this type of response. However, work in this area has mostly been limited to uniaxial material models, for use in conventional fiber elements. In uniaxial material models, the constitutive effects of local buckling may be conveniently represented through an asymmetric stress–strain relationship that has a softening branch on the compression side but hardens monotonically in tension. Mahan et al. (2011) have also used such stress–strain laws to simulate rebar buckling in fiber elements. However, unlike conventional fiber elements, the TFE element uses multiaxial fibers (Fig. 7) with three strain components (ε_{xx},γ_{xy}, and γ_{xz}) as inputs and three stress components (σ_{xx}, τ_{xy}, and τ_{xz} components) as outputs; this necessitates the use of a multiaxial material model. Unfortunately, a multiaxial material model for steel with asymmetric softening (to represent local buckling) is not readily available. As a result, the von Mises plasticity model is calibrated with a softening branch; specifically, an isotropic hardening law is modified to a smoothened trilinear curve, with linear elastic branch, followed by linear hardening, and then linear softening that matches the uniaxial local buckling response of the flange and web. Fig. 12 illustrates such a stress–strain curve calibrated for one of the simulations (simulation #11). The parameters for this representative effective uniaxial stress–strain curve for local buckling are as follows. The elastic modulus E and the yield stress σ_y are set equal to 200 GPa and 345 MPa, respectively, based on material constitutive data. However, the stress σ_u, which represents the initiation of local buckling,depends on flange slenderness (Kolwankar et al. 2018; Suzuki and Lignos 2018). Consequently, the effective buckling stress (σ_u) and corresponding effective strain (ε_u) values were recovered from each of the CFE simulations, following a process outlined by Kolwankar et al. (2018). The other parameter of the softening branch, i.e., the linear post-buckling softening modulus, is also adopted from Kolwankar et al. (2018). All of these parameters are used to calibrate the softening von Mises model in the counterpart TFE simulation. It is well-known (Spacone et al. 1996; Wu and Wang 2010) that softening constitutive properties lead to mesh dependence of the solution, because softening tends to localize in a single element. To mitigate this, Kolwankar et al. (2018) suggested the use of a fixed element size (to set the length scale) at the anticipated plastic hinge regions along with the softening parameters (calibrated for the same length scale) as discussed above. Following these recommendations, an element size of $1.5b_f$ was adopted in this study. Mesh (outside the plastic hinge region) and fiber discretization and the integration rules for the TFE model are similar to that in the LT cases.

It is important to note that the axisymmetry of the von Mises yield surface with respect to the hydrostatic stress (σ_H) [Fig. 12(a)] axis implies that any softening applied to the von Mises material is

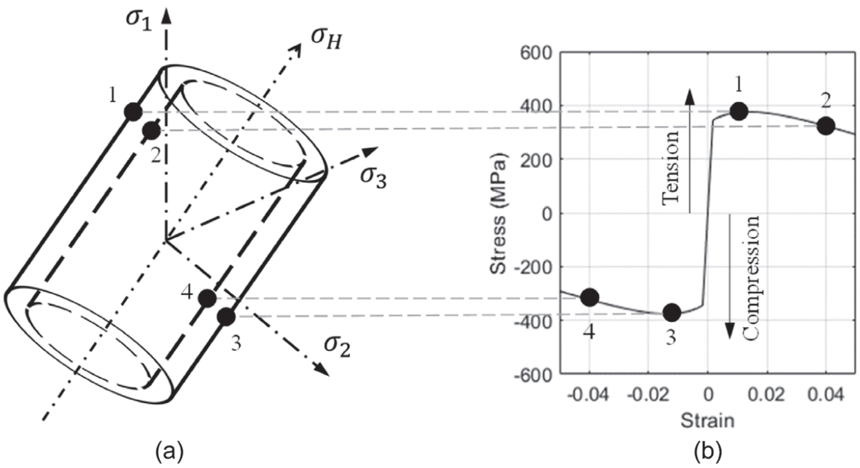

(a) (b)

Fig. 12. Calibrated effective uniaxial stress vs strain curve for J_2 Plasticity model (a) von Mises cylinder in the stress space; and (b) uniaxial stress vs strain response.

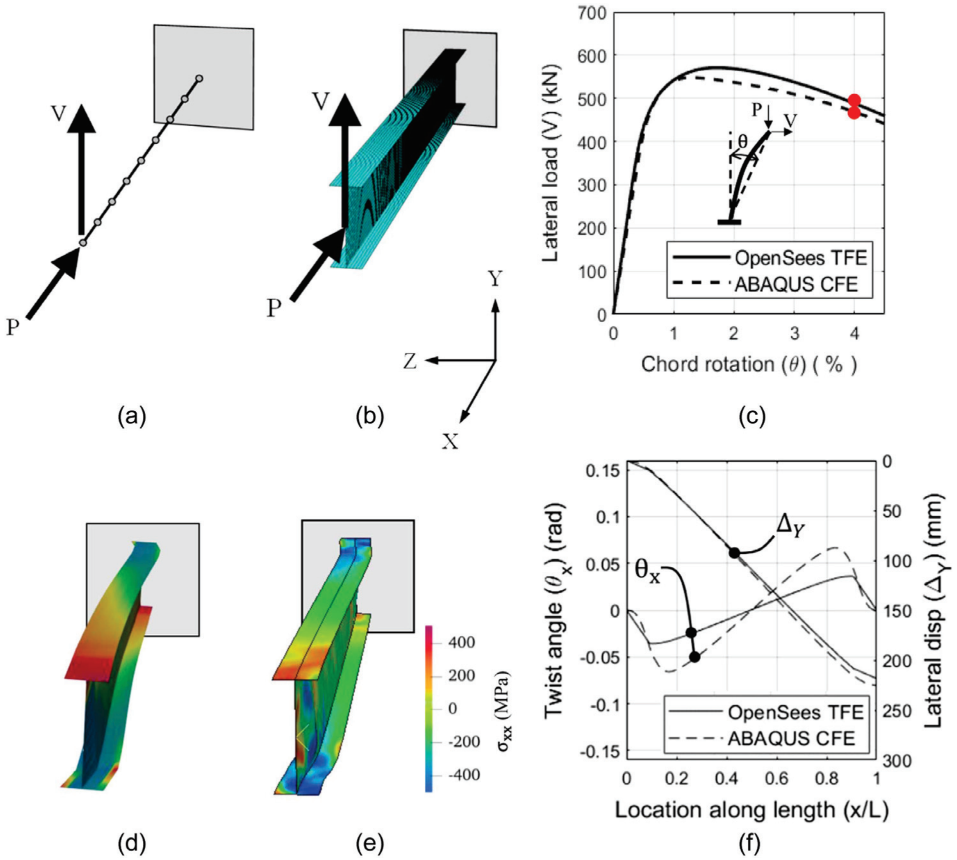

Fig. 13. Comparison between CFE and TFE model results for simulation #18 – W24X103, $P/P_y = 0.3$, Fx-Fx end conditions: (a) TFE model; (b) CFE model (undeformed); (c) comparison of load-deformation curves; (d) deformation profile and σ_{xx} contours from TFE simulation; (e) deformation profile and σ_{xx} contours from CFE simulation; and (f) longitudinal distribution of lateral displacement (Δ_y) and twist angle (θ_x) at the instance shown in the load-deformation curves (4% chord rotation)

symmetrically effective in compression as well as tension. This is clearly a problem because local buckling-induced effective softening does not occur in tension. However, as discussed above, a multiaxial metal plasticity model, which can capture this type of asymmetric behavior is currently unavailable (although it is being developed as part of the broader project that encompasses this study). Despite this issue, the use of the softening von Mises model is informative for two reasons: (1) in practical terms, the symmetric von Mises model appears to be satisfactory to predict response because local buckling on the compression side of the member occurs before the softening branch is engaged on the tension side, due to the net compression in most of the configurations, and (2) perhaps more importantly, the approach provides the opportunity to examine the functional ability of the TFE element formulation to simulate IB which is caused by local buckling induced softening leading to lateral torsional buckling. As improved multiaxial models for local buckling induced softening become available, it is anticipated that they will be used within the TFE element construct for even more effective simulation of IB. Figs. 13(a–f) compare the results of TFE to CFE simulations (Simulation #18 provide the details) loaded under a transverse load. These figures provide a representative assessment of the performance of the TFE element. The observations from Figs. 13(a–f) are similar to those from Figs. 10(a–f) presented previously for the GT configurations; specifically, that:

1. The load-deformation curve, as well as the deformation modes appear to be strikingly similar between the TFE and the CFE models. The TFE model is able to capture the full range of response of observed in the CFE models, ranging from the initial elastoplastic response to local buckling, and then lateral torsional buckling that is triggered by local buckling.
2. The longitudinal distribution of both the transverse deflection and the twist appears to be qualitatively similar between the two. However, the CFE predicts greater twist than the TFE, suggesting a stronger degree of localization. This may be attributed to the length scale (i.e., the element size equal to $1.5b_f$) used for the constitutive softening model in the TFE, originally inferred by Kolwankar et al. (2018) for purely local buckling (no interactive buckling).

As for the LT configurations, Fig. 13 and the above observations describe the response of only one representative case. To examine the efficacy of the TFE model across various configurations, Figs. 14(a–c) plot the error measures $\epsilon_{load-def}$ (similar to the LT case discussed earlier) and ϵ_{Δ_y} (averaged error in lateral displacement along length at a particular drift level) against the parameters $b_f/2t_f$, h/t_w, and L/r_y, respectively, to examine trends within the response of the TFE model. Referring to these figures, it is noted that:

- All the error measures are reasonably low (up to 10%), suggesting that the TFE elements with a calibrated softening multiaxial model can predict the softening response due to IB in an efficient manner.
- The error in load-deformation ($\epsilon_{load-def}$) increases with increasing flange slenderness ratio (beyond the highly ductile limit

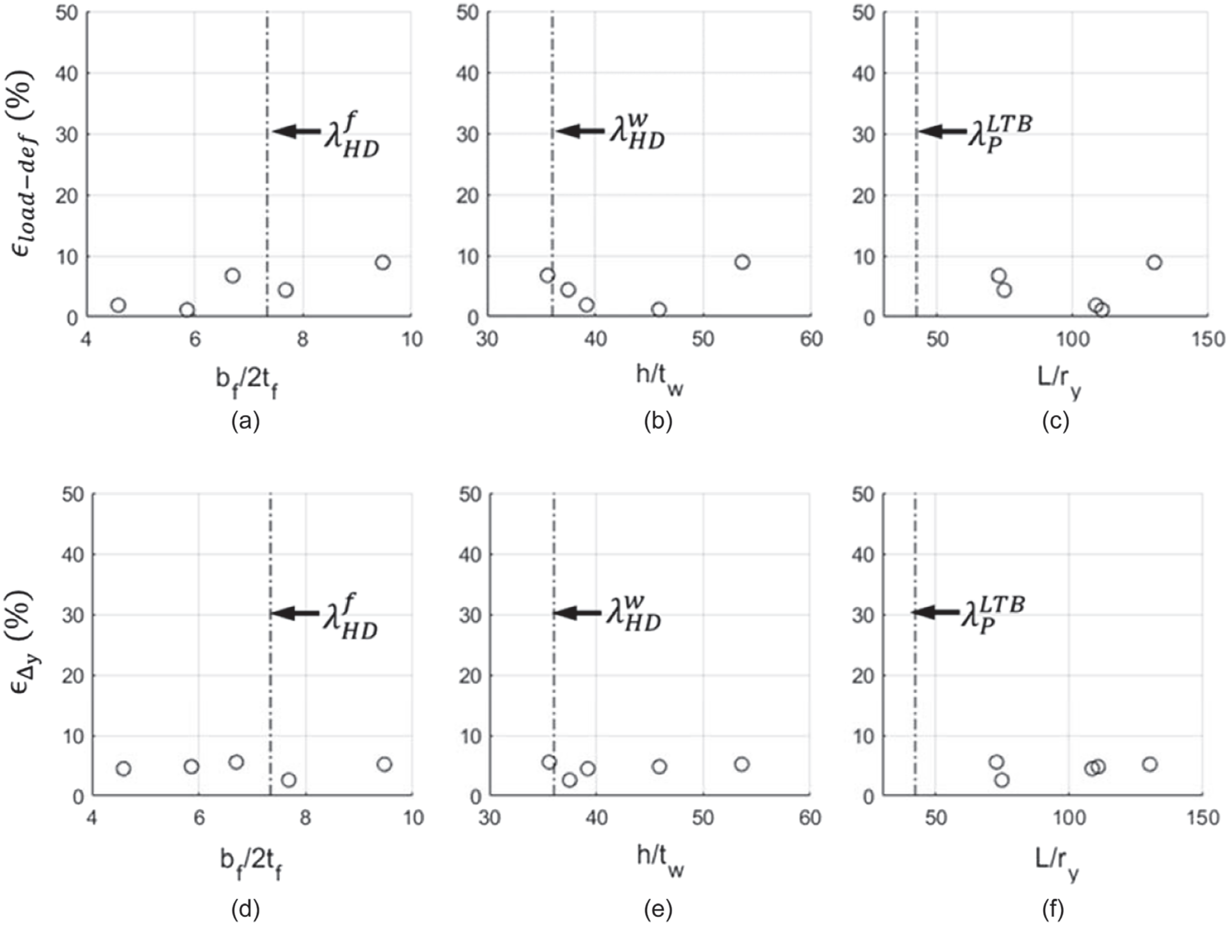

(a) (b) (c)

(d) (e) (f)

Fig. 14. Measured errors vs section and member slenderness ratio plots for IB response cases: (a)–(c) error in load-deformation; and (d)–(f) error in lateral displacement profile (Δ_y)

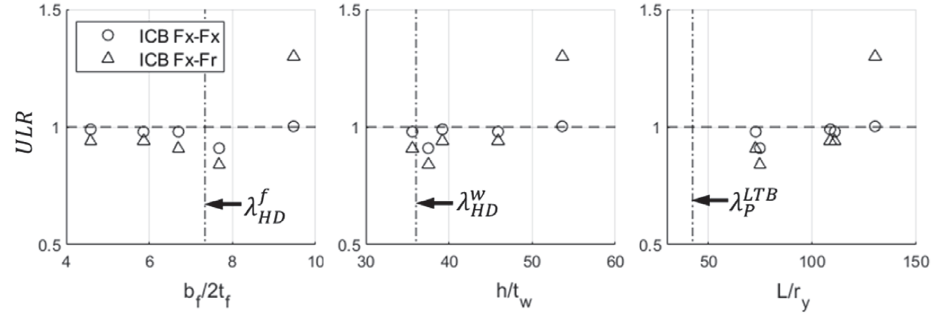

(a) (b) (c)

Fig. 15. Ultimate Load Ratio (ULR) vs section and member slenderness ratio plots for GT and IB response cases.

λ_{HD}^{f}), which is reasonable because of complicated modes in flange local buckling [full wave buckled shape and larger localization zone (~$2.5b_f$)], which may require different length scales depending on the length of the buckled flange.

- The error in the lateral displacement shape (ε_{Δ_y}) is low and consistent for the wide range of chosen slenderness ratio.

Another indicator of the efficacy of the simulations is their ability to predict the ultimate load. Therefore, ultimate load comparisons for both the GT and IB cases ($0.2P_y$ axial load) are summarized in Fig. 15; the Ultimate Load Ratio (ULR) is defined as

$$ULR = \frac{V_{ult}^{TFE}}{V_{ult}^{CFE}}$$

In the above, V_{ult}^{TFE} and V_{ult}^{CFE} are defined as the ultimate loads from the TFE and the CFE simulations respectively. Referring to Fig. 15 (which plots the ULR against measures of local and global slenderness), it is noted that, in general, the predicted ultimate loads through the TFE are fairly close to the CFE (an average ULR of 0.91 and 0.97 for LT and IB, respectively, with a standard deviation of 0.046 and 0.036 for LT and IB, respectively). Interestingly, the ULR shows a modest increase with respect to both local and global slenderness, indicating that the TFE model over-predicts the peak load in these cases, which may be attributed to the somewhat incomplete representation of geometric nonlinear response and material properties mentioned earlier.

Considerations for Simulation of Frames Using the TFE Element

Simulating frames using TFE elements is similar to that using regular 3-d frame elements, with some key differences. Specifically, conventional beam elements only have six degrees of freedom at each node, whose physical interpretations (rotation and displacements) are straightforward. However, when elements with seven (including warping) degrees of freedom are used, the interpretation, and moreover the application of boundary conditions and compatibility constraints between members requires additional discussion. When simulating frame structures with such elements, the following observations are useful:

- At supports (i.e., foundations), it is usually appropriate to represent the warping degree of freedom of the support as fixed. In this regard, it is important to note that the warping deformations may be considered scalars (see kinematic analysis by Desautels 1980; Pignataro et al. 2010), such that prescribing a fixed warping boundary conditions sets the warping deformations at all the members framing into the support as zero (i.e., $\theta_x' = 0$ for all members).
- At free nodes (i.e., where supports are not present), the work-conjugate of the warping deformation (i.e., the bimoment) may be set as zero, such that the node may experience appropriate warping deformations, as a solution of the analysis.
- The points above pertain to boundary conditions (or external restraints). However, it is important to also consider continuity (or lack thereof) of warping deformations among members framing into a single joint. In this context, it is noted that the transmission of the warping deformations across structural connections usually depend on the specific connection detail. For example, a gusset plate connection (between a brace and a column, as an example) will not transmit warping deformations in the same manner as if the brace were welded to the column directly. Consequently, the type of warping continuity to provide at such connections is at the discretion of the user. A common approach is to provide a warping continuous idealization (Murín et al. 2012; Tong et al. 2005), which is applicable in seismically designed moment frames with stiffened joints. However, if more accurate behavior is desired, sophisticated joint models for various types of joints (Basaglia et al. 2012; Krenk and Damkilde 1991; Tong et al. 2005; Vacharajittiphan and Trahair 1974) should be incorporated in the simulation. It is important to note that if such a joint model is used, then additional (free) degrees of freedom will be generated at the junctions between each member framing into the joint, and the element representing the joint.

Summary and Conclusions

The synergistic interactions between local and lateral torsional buckling in steel members is often one of the reasons for their loss of strength, and the collapse of structures. However, prevalent frameworks for simulating this type of response rely largely on phenomenological approaches wherein concentrated hinge or fiber models are calibrated to match overall load-deformation response. Since these approaches do not represent the underlying physical phenomena, they are challenging to generalize and prone to inaccuracy. To address this, a new beam-column element formulation, termed the Torsional Fiber Element (TFE) is proposed. The aim of this element is to be able to functionally represent the phenomena that are responsible for IB, to enable prediction of such response in a general manner. To enable this, the TFE has four key features: (1) enrichment of strain and deformation interpolation functions to represent deformation modes associated with warping and St. Venant torsion in addition to axial and flexural loading, (2) an updated Lagrangian approach to capture geometric nonlinearity and instability arising from these deformation modes, (3) the use of multiaxial fiber plasticity to incorporate the interactions between axial and shear stresses in inducing plasticity and buckling, and (4) representation of local buckling through an effective softening constitutive response. The formulation is implemented in the open-source software OpenSees version 3.0.0a, and its results are examined against counterpart results of 38 CFE simulations and one experiment. The comparisons indicate that: (1) the TFE is able to functionally represent the fundamental physical phenomena and deformation modes that underlie local, lateral torsional, and IB. The TFE element appears to successfully simulate the load-deformation response, as well as local deformation patterns and stress/strain distributions with good accuracy.

While the approach shows promise in simulating IB in frame members, in its current form, the TFE has several limitations that are the subject of ongoing or future study; these are briefly summarized here. First, the TFE element has been developed and demonstrated only for monotonic loading conditions. Although the element formulation is generally applicable to cyclic loading as well, aspects of it may require modifications especially if cyclically evolving stress/strain fields over the element diverge from those assumed in the interpolation functions. Second, a von Mises plasticity model with a softening branch was used to represent effective softening due to local buckling; this is inconsistent with actual response because it is symmetric (i.e., softening in both tension and compression, rather than just in compression); this is an inherent feature of von Mises plasticity which cannot be circumvented until a more appropriate multiaxial constitutive model is developed. Nonetheless, it is used to demonstrate the functional abilities of the TFE element to predict IB. Third, softening constitutive response results in mesh dependence, which must be regularized through the introduction of a length scale for localization. In this study, this was done through pre-selecting the element size to be $1.5b_f$. This is an expedient approach, but not a particularly attractive one, because the user must select the mesh size in concert with the constitutive properties. Based upon previous work by the authors (Kolwankar et al. 2018, 2020), development of a nonlocal formulation for the TFE to mitigate this problem is currently underway. In closing, while TFE element has these limitations, it also possesses the fundamental characteristics to simulate the phenomena responsible for IB, and in its current form. is able to simulate monotonic inelastic lateral torsional response, as well as IB with success. Mitigation of these shortcomings will result in an element highly useful for simulating collapse of steel structures.

Data Availability Statement

Some or all data, models, or code that support the findings of this study are available from the corresponding author upon reasonable request.

Acknowledgments

The work was supported by the US National Science Foundation (Grant # CMMI-1926202) and by the Suisse National Science Foundation (Award Number: 200021_188476), and an internal research grant from École Polytechnique Fédérale de Lausanne. The findings and opinions presented in this paper are entirely those of the authors.

References

AISC. 1997. "Torsional analysis of structural steel members." In *Steel design guide 9*. Chicago, IL: AISC.

AISC. 2016a. *Specification for structural steel buildings*. ANSI/AISC 360-16. Chicago, IL: AISC.

AISC. 2016b. *Seismic provisions for structural steel buildings*. ANSI/AISC 341-16. Chicago, IL: AISC.

ASCE. 2017. *Minimum design loads and associated criteria for buildings and other structures*. ASCE/SEI 7-16. Reston, VA: ASCE.

Basaglia, C., D. Camotim, and N. Silvestre. 2012. "Torsion warping transmission at thin-walled frame joints: Kinematics, modelling and structural response." *J. Constr. Steel Res.* 69 (1): 39–53. https://doi.org/10.1016/j.jcsr.2011.07.016.

Bathe, K.-J., and P. M. Wiener. 1983. "On elastic-plastic analysis of I-beams in bending and torsion." In *Proc., Nonlinear Finite Element Analysis and Adina*, 711–718. Cambridge, MA: Pergamon.

Chansuk, P., G. Ozkula, C.-M. Uang, and J. L. Harris. 2021. *Seismic behavior and design of deep, slender wide-flange structural steel beam-columns*. Gaithersburg, MD: NIST.

Cravero, J., A. Elkady, and D. G. Lignos. 2020. "Experimental evaluation and numerical modeling of wide-flange steel columns subjected to constant and variable axial load coupled with lateral drift demands." *J. Struct. Eng.* 146 (3): 04019222. https://doi.org/10.1061/(ASCE)ST.1943-541X.0002499.

Desautels, P. 1980. *Elasto-plastic torsion of thin-walled members*. Montreal: McGill Univ.

Dides, M. A., and J. C. de la Llera. 2005. "A comparative study of concentrated plasticity models in dynamic analysis of building structures." *Earthquake Eng. Struct. Dyn.* 34 (8): 1005–1026. https://doi.org/10.1002/eqe.468.

Du, X., and J. Hajjar. 2021. "Three-dimensional nonlinear displacement-based beam element for members with angle and tee sections." *Eng. Struct.* 239 (Jul): 112239. https://doi.org/10.1016/j.engstruct.2021.112239.

Elkady, A. 2016. *Collapse risk assessment of steel moment resisting frames designed with deep wide-flange columns in seismic regions*. Montreal: McGill Univ.

Elkady, A., and D. G. Lignos. 2015. "Analytical investigation of the cyclic behavior and plastic hinge formation in deep wide-flange steel beam-columns." *Bull. Earthquake Eng.* 13 (4): 1097–1118. https://doi.org/10.1007/s10518-014-9640-y.

Elkady, A., and D. G. Lignos. 2018a. "Full-scale testing of deep wide-flange steel columns under multiaxis cyclic loading: Loading sequence, boundary effects, and lateral stability bracing force demands." *J. Struct. Eng.* 144 (2): 04017189. https://doi.org/10.1061/(ASCE)ST.1943-541X.0001937.

Elkady, A., and D. G. Lignos. 2018b. "Improved seismic design and nonlinear modeling recommendations for wide-flange steel columns." *J. Struct. Eng.* 144 (9): 04018162. https://doi.org/10.1061/(ASCE)ST.1943-541X.0002166.

Farwell, C. R., and T. V. Galambos. 1969. "Nonuniform torsion of steel beams in inelastic range." *J. Struct. Div.* 95 (12): 2813–2830. https://doi.org/10.1061/JSDEAG.0002438.

Felippa, C. A. 2000. *A systematic approach to the element independent corotational dynamics of finite elements*. Boulder, CO: Univ. of Colorado.

FEMA. 2009. *Quantification of building seismic performance factors*. FEMA-P695. Washington, DC: FEMA.

Fieber, A., L. Gardner, and L. Macorini. 2019. "Design of structural steel members by advanced inelastic analysis with strain limits." *Eng. Struct.* 199 (Nov): 109624. https://doi.org/10.1016/j.engstruct.2019.109624.

Fogarty, J., and S. El-Tawil. 2016. "Collapse resistance of steel columns under combined axial and lateral loading." *J. Struct. Eng.* 142 (1): 04015091. https://doi.org/10.1061/(ASCE)ST.1943-541X.0001350.

Fukumoto, Y., and T. V. Galambos. 1966. "Inelastic lateral-torsional buckling of beam-columns." *J. Struct. Div.* 92 (2): 41–62. https://doi.org/10.1061/JSDEAG.0001442.

Hajjar, J. F., P. H. Schiller, and A. Molodan. 1998. "A distributed plasticity model for concrete-filled steel tube beam-columns with interlayer slip." *Eng. Struct.* 20 (8): 663–676. https://doi.org/10.1016/S0141-0296(97)00107-7.

Ibarra, L. F., R. A. Medina, and H. Krawinkler. 2005. "Hysteretic models that incorporate strength and stiffness deterioration." *Earthquake Eng. Struct. Dyn.* 34 (12): 1489–1511. https://doi.org/10.1002/eqe.495.

Kemp, A. R. 1996. "Inelastic local and lateral buckling in design codes." *J. Struct. Eng.* 122 (4): 374–382. https://doi.org/10.1061/(ASCE)0733-9445(1996)122:4(374).

Kircher, C., G. Deierlein, J. Hooper, H. Krawinkler, S. Mahin, B. Shing, and J. Wallace. 2010. *Evaluation of the FEMA P-695 methodology for quantification of building seismic performance factors*. Gaithersburg, MD: NIST.

Kolwankar, S., A. Kanvinde, M. Kenawy, D. G. Lignos, and S. K. Kunnath. 2018. "Simulating local buckling-induced softening in steel members using an equivalent nonlocal material model in displacement-based fiber elements." *J. Struct. Eng.* 144 (10): 04018192. https://doi.org/10.1061/(ASCE)ST.1943-541X.0002189.

Kolwankar, S., A. Kanvinde, M. Kenawy, D. G. Lignos, and S. K. Kunnath. 2020. "Simulating cyclic local buckling–induced softening in steel beam-columns using a nonlocal material model in displacement-based fiber elements." *J. Struct. Eng.* 146 (1): 04019174. https://doi.org/10.1061/(ASCE)ST.1943-541X.0002457.

Krenk, S., and L. Damkilde. 1991. "Warping of joints in I-Beam assemblages." *J. Eng. Mech.* 117 (11): 2457–2474. https://doi.org/10.1061/(ASCE)0733-9399(1991)117:11(2457).

Krishnan, S. 2010. "Modified elastofiber element for steel slender column and brace modeling." *J. Struct. Eng.* 136 (11): 1350–1366. https://doi.org/10.1061/(ASCE)ST.1943-541X.0000238.

Le Corvec, V. 2012. *Nonlinear 3d frame element with multi-axial coupling under consideration of local effects*. Berkeley, CA: UC Berkeley.

Le Corvec, V., and F. C. Filippou. 2011. "Enhanced 3d fiber beam-column element with warping displacements." In *Proc., 3rd ECCOMAS Thematic Conf. on Computational Methods in Structural Dynamics and Earthquake Engineering*. Athens, Greece: National Technical Univ. of Athens.

Lemaitre, J., and J. L. Chaboche. 1990. *Mechanics of solid materials*. Cambridge, UK: Cambridge University Press.

Mahan, M., Y. F. Dafalias, M. Taiebat, Y. Heo, and S. K. Kunnath. 2011. "SANISTEEL: Simple anisotropic steel plasticity model." *J. Struct. Eng.* 137 (2): 185–194. https://doi.org/10.1061/(ASCE)ST.1943-541X.0000297.

McGuire, W., R. H. Gallagher, and R. D. Ziemian. 2000. *Matrix structural analysis*. New York: Wiley.

Murín, J., V. Kutiš, V. Královič, and T. Sedlár. 2012. "3D beam finite element including nonuniform torsion." *Procedia Eng.* 48 (Jan): 436–444. https://doi.org/10.1016/j.proeng.2012.09.537.

Newell, J. D., and C.-M. Uang. 2008. "Cyclic behavior of steel wide-flange columns subjected to large drift." *J. Struct. Eng.* 134 (8): 1334–1342. https://doi.org/10.1061/(ASCE)0733-9445(2008)134:8(1334).

NIST. 2017a. *Guidelines for nonlinear structural analysis and design of buildings. Part IIa–Steel moment frames*. NIST GCR 17-917-46v2. Gaithersburg, MD: NIST.

NIST. 2017b. *Guidelines for nonlinear structural analysis and design of buildings. Part IIb - Reinforced concrete moment frames*. NIST GCR 17-917-46v3. Gaithersburg, MD: NIST.

PEER/ATC. 2010. *Modeling and acceptance criteria for seismic design and analysis of tall buildings*. PEER/ATC-72-1. Redwood City, CA: ATC.

Pi, Y. L., and N. S. Trahair. 1994a. "Nonlinear inelastic analysis of steel beam-columns. I: Theory." *J. Struct. Eng.* 120 (7): 2041–2061. https://doi.org/10.1061/(ASCE)0733-9445(1994)120:7(2041).

Pi, Y. L., and N. S. Trahair. 1994b. "Nonlinear inelastic analysis of steel beam-columns. II: Applications." *J. Struct. Eng.* 120 (7): 2062–2085. https://doi.org/10.1061/(ASCE)0733-9445(1994)120:7(2062).

Pi, Y. L., and N. S. Trahair. 1995. "Inelastic torsion of steel I-beams." *J. Struct. Eng.* 121 (4): 609–620. https://doi.org/10.1061/(ASCE)0733-9445(1995)121:4(609).

Pignataro, M., N. Rizzi, G. Ruta, and V. Varano. 2010. "The effects of warping constraints on the buckling of thin-walled structures." *J. Mech. Mater. Struct.* 4 (10): 1711–1727. https://doi.org/10.2140/jomms.2009.4.1711.

Simo, J. C., and L. Vu-Quoc. 1991. "A geometrically-exact rod model incorporating shear and torsion-warping deformation." *Int. J. Solids Struct.* 27 (3): 371–393. https://doi.org/10.1016/0020-7683(91)90089-X.

Spacone, E., F. C. Filippou, and F. F. Taucer. 1996. "Fibre beam–column model for non-linear analysis of R/C frames: Part I. Formulation." *Earthquake Eng. Struct. Dyn.* 25 (7): 711–725. https://doi.org/10.1002/(SICI)1096-9845(199607)25:7<711::AID-EQE576>3.0.CO;2-9.

Subramanian, L. P., and D. W. White. 2015. "Evaluation of lateral torsional buckling resistance equations in AISC and AASHTO." In *Proc., Annual Stability Conf.* Nashville, TN: SSRC.

Suzuki, Y., and D. G. Lignos. 2018. "Fiber-based model for earthquake-induced collapse simulation of steel frame buildings." In *Proc., 11th U.S. National Conf. on Earthquake Engineering*. Los Angeles: EERI.

Suzuki, Y., and D. G. Lignos. 2021. "Experimental evaluation of steel columns under seismic hazard-consistent collapse loading protocols." *J. Struct. Eng.* 147 (4): 04021020. https://doi.org/10.1061/(ASCE)ST.1943-541X.0002963.

Timoshenko, S. P. 1945. "Theory of bending, torsion and buckling of thin-walled members of open cross section." *J. Franklin Inst.* 239 (5): 343–361. https://doi.org/10.1016/0016-0032(45)90013-5.

Tong, G. S., X. X. Yan, and L. Zhang. 2005. "Warping and bimoment transmission through diagonally stiffened beam-to-column joints." *J. Constr. Steel Res.* 61 (6): 749–763. https://doi.org/10.1016/j.jcsr.2004.12.002.

Vacharajittiphan, P., and N. S. Trahair. 1974. "Warping and distortion at I-section joints." *J. Struct. Div.* 100 (3): 547–564. https://doi.org/10.1061/JSDEAG.0003738.

White, M. W. 1956. *The lateral-torsional buckling of yielded structural steel members*. Bethlehem, PA: Lehigh Univ.

Wu, S., and X. Wang. 2010. "Mesh dependence and nonlocal regularization of one-dimensional strain softening plasticity." *J. Eng. Mech.* 136 (11): 1354–1365. https://doi.org/10.1061/(ASCE)EM.1943-7889.0000184.

Wu, T.-Y., S. El-Tawil, and J. McCormick. 2018. "Seismic collapse response of steel moment frames with deep columns." *J. Struct. Eng.* 144 (9): 04018145. https://doi.org/10.1061/(ASCE)ST.1943-541X.0002150.

Yang, Y. B., S. P. Lin, and L. J. Leu. 2007. "Solution strategy and rigid element for nonlinear analysis of elastically structures based on updated Lagrangian formulation." *Eng. Struct.* 29 (6): 1189–1200. https://doi.org/10.1016/j.engstruct.2006.08.015.